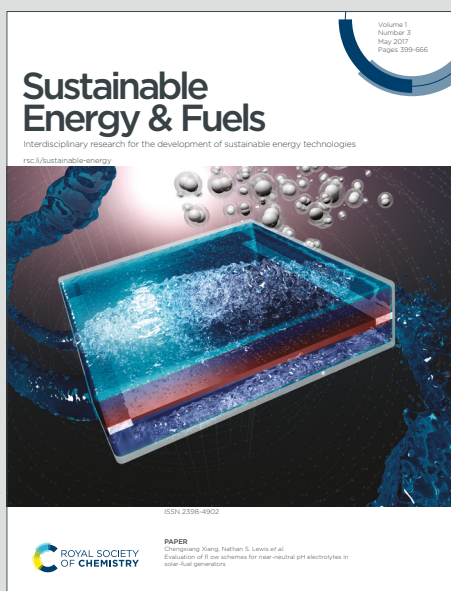Sustainable
Energy & Fuels

Interdisciplinary research for the development of sustainable energy technologies

rsc.li/sustainable-energy

Volume 1
Number 3
May 2017
Pages 399-666

ISSN 2398-4902

ROYAL SOCIETY
OF CHEMISTRY

PAPER
Chengxiang Xiang, Nathan S. Lewis et al.
Evaluation of flow schemes for near-neutral pH electrolytes in solar-fuel generators

ROYAL SOCIETY
OF CHEMISTRY

rsc.li/sustainable-energy

1   **Solventless hydrodeoxygenation of isoeugenol and dihydroeugenol**

2   **in the batch and continuous modes over zeolite-supported FeNi**

3   **catalyst**

4   Zuzana Vajglová[1], Olha Yevdokimova[1], Ananias Medina[1], Kari Eränen[1], Teija Tirri[1],

5   Jarl Hemming[1], Johan Lindén[2], Ilari Angervo[3], Pia Damlin[4],

6   Dmitry E. Doronkin[5], Päivi Mäki-Arvela[1], Dmitry Yu. Murzin[1]*

7   [1] *Åbo Akademi University, Johan Gadolin Process Chemistry Centre, Henriksgatan 2, 20500, Turku/Åbo, Finland*
8   [2] *Faculty of Science and Engineering/Physics, Åbo Akademi University, Henriksgatan 2, 20520, Turku/Åbo,*
9   *Finland*
10   [3] *Wihuri Physical Laboratory, University of Turku, 20014, Turku, Finland*
11   [4] *Department of Material Chemistry, University of Turku, 20014, Turku, Finland*
12   [5] *Institute of Chemical Technology and Polymer Chemistry and Institute of Catalysis Research and Technology,*
13   *Karlsruhe Institute of Technology, Kaiserstrasse 12, 76131, Karlsruhe, Germany*
14   *dmurzin@abo.fi, corresponding author
15

16   **Abstract**

17   A low-cost bimetallic bifunctional 5-5 wt% FeNi/H-Beta-300 catalyst was investigated in

18   solventless hydrodeoxygenation of lignin-derived model compounds isoeugenol or

19   dihydroeugenol in the batch and continuous mode. The catalyst was characterized in detail by

20   laser diffraction, scanning electron microscopy – energy dispersive X-ray microanalysis,

21   inductively couple plasma – optical emission spectrometry, transmission electron microscopy,

22   Fourier-transform infrared spectroscopy with pyridine, X-ray diffraction, Mössbauer

23   spectroscopy, X-ray absorption spectroscopy, hydrogen temperature programmed reduction,

24   nitrogen physisorption, thermogravimetric analysis, oxygen temperature programmed

25   oxidation, organic elemental analysis, soluble coke extraction by dichloromethane, and Raman

26   spectroscopy. The composition of the reaction mixture was analysed by GC-FID, GC-MS, SEC

27   and Karl-Fischer titration, while microGC-TCD was used for analysis of the gas phase.

28   Selectivity of 80% to the desired oxygen-free compounds was obtained at ca 80% of the initial

29   dihydroeugenol conversion with 0.3 g of catalyst at 300 °C and 30 bar of hydrogen with a

30   residence time of 12 min. Catalyst deactivation occurred via aliphatic coke formation which

31   resulted not only in a decrease of conversion but also significant selectivity changes with

32   increasing time-on-stream. The apparent activation energy of dihydroeugenol

33   hydrodeoxygenation in solventless isoeugenol hydrodeoxygenation was calculated to be 6.3

34   kJ/mol ascribed to both external mass transfer limitations of hydrogen dissolved in

35   dihydroeugenol and by rapid catalyst deactivation in the initial isoeugenol hydrogenation. The

36   spent catalyst was successfully regenerated by coke oxidation and subsequently reused.

37

1 Introduction

Substitution of petroleum with fuels obtained from renewable sources, such as bio-oil is an important step to prevent many environmental problems, including global warming. Because bio-oils have high acidity and oxygen content as well as low stability, they are not suitable to be used directly as fuels. Hydrodeoxygenation (HDO) is a cheap way to improve quality of fuels from bio-oil by removing oxygen from the oxygen-containing compounds. HDO is the most commonly used method to upgrade bio-oil to deoxygenated hydrocarbon fuels, which have higher stability and energy density.[1] Bio-oil consists of an aqueous and organic phase with the latter containing various acids, aldehydes, ketones and phenolic components, reflecting the complex nature of lignocellulosic biomass. Due to this complexity typically model compounds are used to study the reaction mechanism of HDO and its kinetics. Isoeugenol (IE) and its hydrogenated product, dihydroeugenol (DHE) are used in this work as model compounds, because isoeugenol containing hydroxyl, methoxy and allyl groups, also found in bio-oils derived from lignin, can be considered as a representative lignin model compound.[1,2]

Batch-wise HDO of lignin derived compounds was already performed with noble,[1,3,4] noble metal containing bimetallic catalysts[5,6] and non-noble metal-based catalysts[2,3,7]. As there is an increased interest in industry to use cheap non-noble metal materials as catalysts, abundant Fe and Ni were selected as active metals. It has been already reported, that HDO of triolein was successfully performed over a bifunctional Ni–Fe/ZSM-5/SAPO-11 catalyst, which displayed higher catalytic activity than monometallic ones.[7] Fe is oxophilic metal, which promotes oxygen adsorption and subsequently activity and selectivity in HDO of oxygen containing compounds.[8] Despite few attempts reported in the literature, there is not much information about application of non-noble bimetallic catalysts for HDO of lignin-derived compounds. Furthermore, it is known that acidity, structure and morphology of a support can influence

63   catalytic activity,[9] with strong acidity eventually resulting in cracking and catalyst deactivation.

64   Subsequently in the current work, mildly acidic Beta-300 was chosen as a support.

65   The aim in the current work was to compare the performance of a bimetallic bifunctional

66   5-5 wt% FeNi/H-Beta-300 in batch and continuous reactors. According to our knowledge

67   continuous HDO of similar components has been previously made in the gas-phase,[10] and the

68   open literature is almost devoid of studies performed in the liquid–phase when IE and DHE are

69   used as a feedstock in solvent-less conditions. A comprehensive product analysis was

70   performed including the liquid, solid and gas phase analysis. One of the aims of the current

71   research was to elucidate catalyst stability in the absence of any solvent, as the latter ones,

72   especially long chain hydrocarbons, are not inert under the reaction conditions.[11] Furthermore,

73   several physico-chemical methods were applied to characterize the fresh and spent catalysts,

74   such as laser diffraction, scanning electron microscopy – energy dispersive X-ray

75   microanalysis, inductively coupled plasma – optical emission spectrometry, transmission

76   electron microscopy, Fourier-transform infrared spectroscopy with pyridine, X-ray diffraction,

77   Mössbauer spectroscopy, X-ray absorption spectroscopy, hydrogen temperature programmed

78   reduction, nitrogen physisorption, thermogravimetric analysis, oxygen temperature

79   programmed oxidation, organic elemental analysis, soluble coke extraction by

80   dichloromethane, and Raman spectroscopy.

2 Experimental

2.1   Preparation of the catalyst

83   In the current work, a low-cost bimetallic bifunctional 5-5 wt% FeNi/H-Beta-300 catalyst

84   was synthesised by the subsequent incipient wetness impregnation method with two

85   impregnation steps for each metal. The metal composition was selected based on the results of

86   the previous work dealing with Fe-Ni metal ratios in the catalyst for co-processing of n-

87 hexadecane with lignin derived isoeugenol, resulting in complete deoxygenation over 5 wt%

88 Fe–5 wt% Ni/H-Y-5.1.[11] First, a commercial H-Beta-300 zeolitic support (CP811C-300,

89 Zeolyst International) was pretreated in a muffle oven with a step calcination procedure:

90 temperature ramp at 4 °C/min rate to 250 °C (held for 50 min), increased at 2 °C/min to 500 °C

91 (held for 4 h). First iron and then nickel were subsequently introduced using a 1.6 M aqueous

92 solution of $Fe(NO_3)_3 \cdot 9H_2O$ (Sigma-Aldrich) and a 1.5 M $Ni(NO_3)_2 \cdot 6H_2O$ (CJSC

93 Souzchimprom) precursors, respectively. After each impregnation step, the sample was dried

94 at 100 °C overnight, and the final sample with 10 wt% of the total metal nominal loading was

95 calcined at 450 °C for 6 h under static air. Before the catalytic experiment, the catalyst was

96 reduced in the flow of hydrogen, 40 mL/min, with the heating rate of 2 °C/min to 250 °C (held

97 for 2h) and subsequently to 500 °C (held for 2 h).

2.2 Characterization of the catalyst

99 Fresh and spent FeNi/H-Beta-300 catalysts were characterized by a range of physico-

100 chemical methods. The fresh catalyst for characterization was pre-reduced ex-situ with the same

101 reduction program as used before the catalytic experiments. Most of details of characterization

102 methods and the corresponding equipment are given in the previous publications[11,12] with the

103 pertinent details presented below.

2.2.1 Catalyst particle size distribution

105 The catalyst particle size distribution was determined by Malvern Mastersizer 3000 laser

106 diffractometer. The catalyst was dispersed in distilled water using a Hydro EV wet sample

107 dispersion unit.

108   *2.2.2 Surface morphology*

109   The surface morphology and the shape of the sieved catalyst particles were analysed by

110   scanning electron microscopy (SEM, Zeiss Leo Gemini 1530) with a SE (secondary electron),

111   a BSE (back-scattered electron), and an In-Lens detector.

112   *2.2.3 Elemental analysis*

113   Chemical composition of the catalyst bulk was studied by energy dispersive X-ray

114   microanalysis (EDX, Zeiss Leo Gemini 1530). The concentration of metals in the bulk of the

115   catalyst was analyzed by inductively couple plasma – optical emission spectrometry (ICP-OES,

116   PerkinElmer Optima 5300 DV instrument).

117   *2.2.4 Metal particle sizes*

118   The metals particle sizes were analysed by transmission electron microscopy (TEM, Jeol

119   JEM-1400Plus) and measured by Fiji ImageJ software.[13]

120   *2.2.5 Brønsted and Lewis acid sites*

121   The catalyst acidity was measured by Fourier-transform infrared spectroscopy (ATI Mattson

122   FTIR) using pyridine ($\geq$ 99.5%, a.r.) as a probe molecule for determination of the amount and

123   strength of both Brønsted and Lewis acid sites.

124   *2.2.6 Phase identification and the metal valence state composition*

125   X-ray diffraction (XRD) characterisation was used to investigate the phase purity and crystal

126   phase identification by PANalytical Empyrean diffractometer with five-axis goniometers.

127   The Fe valence state composition in the bulk was investigated by Mössbauer spectroscopy.

128   The ^{57}Fe Mössbauer spectra were acquired at 295 K using an 18-month-old ^{57}Co:Rh source

129   (Ritverc Co. 50 mCi June 2020) with a maximum Doppler velocity of 11.0 mm/s.

130   X-ray absorption spectroscopy, in terms of X-ray absorption near edge structure (XANES)

131   and extended X-ray absorption fine structure (EXAFS), was used to study the bulk-averaged

132   element specific local structure around Fe and Ni atoms. Measurements were performed on the

133   as received (calcined) and reduced (in situ) fresh catalyst and also on the as-received (stored in

134   air) and reduced (quasi in situ) spent catalyst, used in isoeugenol HDO in the batch reactor. For

135   reduction the catalyst samples were placed in a quartz capillary, 1.5 mm o.d., 0.02 mm wall

136   thickness, sample bed length 3 mm. Pure H_2 was flowing through the samples at 20 ml/min

137   flow rate which were heated by a hot air blower from 0 to 250 °C with a dwell time of 2 h and

138   subsequently from 250 to 500 °C (2 h dwell time) with the temperature ramp of 2 °C/min (same

139   temperature program as before the catalytic tests). After that the fresh sample was directly

140   measured (in situ) while the spent sample holder was sealed by means of two-way valves

141   (Swagelok), packed in polyethylene bags using a vacuum food sealer, and transported for the

142   measurements taking place approx. 48 hours later (quasi in situ). XAS spectra at Fe and Ni K

143   absorption edges were recorded at the P65 beamline of PETRA III synchrotron radiation source

144   (DESY, Hamburg) in the transmission mode. Higher harmonics were rejected by a pair of Si

145   plane mirrors installed in front of the monochromator. The energy of the X-ray photons was

146   selected by a Si (111) double-crystal monochromator and the beam size was set by means of

147   slits to 0.3 (vertical) x 1.5 (horizontal) mm^2. X-ray absorption near edge spectra (XANES) were

148   normalized and the extended X-ray absorption fine structure spectra (EXAFS) background

149   subtracted using the Athena program from the IFEFFIT software package.[14] The k^2-weighted

150   EXAFS functions were Fourier transformed (FT) in the k range of $2 - 14$ $Å^{-1}$ and multiplied by

151   a Hanning window with the sill size of 1 $Å^{-1}$. The displayed FT EXAFS spectra were not

152   corrected for the phase shift. Amplitude reduction factors S_0^2 0.65 (Fe) and 0.81 (Ni) were

153   obtained by fitting the Fe and Ni foil reference spectra. The fits of the EXAFS data were

154   performed using Artemis software[14] by a least square method in R-space between 1.0 and 3.0

155   Å. Coordination numbers (CN), interatomic distances (r), energy shift (δE_0) and the mean

156   square deviation of interatomic distances (σ^2) were refined during fitting. The absolute misfit

157   between the theory and the experiment was expressed by ρ.

2.2.7 Reducibility

159   Microtrac Belcat II equipment was used to perform temperature programmed reduction

160   (TPR) measurements. The heating rate for TPR was 5 °C/min (up to 800 °C) under 5 vol%

161   hydrogen in argon.

2.2.8 Textural properties

163   The nitrogen physisorption (Micromeritics 3Flex-3500) was used to determine the textural

164   properties. The surface area and pore size distribution were calculated by Dubinin-

165   Radushkevich (D-R) and the non-local density functional (DFT) methods, respectively.

2.2.9 Coke analysis

167   Thermogravimetric analysis (TGA, SDT650 instrument) was used to detect the mass of

168   heavy compounds adsorbed on the catalyst (coke) after the reaction. The heating rate was 10

169   °C/min (up to 800 °C for 1 min) under air atmosphere.

170   Microtrac Belcat II equipment was used to perform temperature programmed oxidation (O_2-

171   TPO) measurements. The two different heating rates for TPO was used: 5 °C/min (up to 900

172   °C for 10 min) and 2 °C/min (up to 400 °C for 20 min) under 5 vol% oxygen in argon.

173   CHNS analysis were performed at 950 °C using Thermo Fisher ScientificFlash 2000 Organic

174   Elemental Analyzer equipped with TC detector. Cystine, 2,5-bis(5-tert-butyl-benzoxazol-2-

175   yl)thiophene, sulphanilimide and methionine were used as standards.

176   The soluble coke in the spent catalyst was identified by extraction with CH_2Cl_2. Extracts

177   (organic phase) were analyzed by GC-MS (Agilent GC/MS 6890N/5973) using the same

178   column and the same temperature program (held for 10 extra minutes) as for the reaction

179   product analysis.

180   Raman spectroscopy was carried out using the Renishaw inVia Qontor confocal Raman

181   microscope system with Raman mapping and a focus track capability. The Raman microscope

182   was equipped with four laser lines, ranging from near-IR (785 nm) to visible (633 and 532 nm)

183   and near-UV (355 nm). In the current work, an external laser with wavelengths of 514 nm and

184   1064 nm was also employed.

185   **2.3   Chemicals**

186   The following chemicals were used in the current work: isoeugenol (mixture of cis and trans,

187   99% FG, As $\leq$ 3 ppm, Hg $\leq$ 1 ppm, Cd $\leq$ 1 ppm, Pb $\leq$ 10 ppm, Sigma-Aldrich), dihydroeugenol

188   ($\geq$ 99% FG, As $\leq$ 3 ppm, Hg $\leq$ 1 ppm, Cd $\leq$ 1 ppm, Pb $\leq$ 10 ppm, Sigma-Aldrich), hydrogen

189   (N50, 99.999%, Woikoski Oy), argon (N50, 99.999%, Woikoski Oy), helium (N46, 99.996%,

190   Woikoski Oy), oxygen in argon (5 vol.%, Woikoski Oy), propylcyclohexane (99%, Sigma-

191   Aldrich), hexane ($\geq$ 99%, Fluka), cyclohexane ($\geq$ 99.9%, Alfa Aesar), 2,5-dimethylhexane

192   (99%, Sigma-Aldrich), ethylbenzene ($\geq$ 99.5%, Merck), N,O-bis(trimethylsilyl)-

193   trifluoroacetamide (BSTFA, >=99%, Sigma-Aldrich), tetrahydrofuran (anhydrous, $\geq$99.9%,

194   Merck), mixture of alkanes (Woikoski Oy): ethane (0.9985 mol%), methane (0.9965 mol%),

195   isobutene (1.0053 mol%), n-butane (1.0036 mol%) in helium (96.00 mol%), mixture of alkenes

196   (Woikoski Oy): 1-butene (1.0060 mol%), ethylene (0.9974 mol%), propylene (1.0035 mol%),

197   isobutane (1.0060 mol%) in helium (95.99 mol%), mixture of gases (Woikoski Oy): carbon

198   monoxide (1.05 mol%), carbon dioxide (1.04 mol%), hydrogen (1.07 mol%) in helium (96.84

199   mol%).

200   **2.4   Catalytic tests**

201   Solventless experiments of hydrodeoxygenation were performed with the lignin-derived

202   model compound isoeugenol or dihydroeugenol over 5-5 wt% FeNi/H-Beta-300. The catalyst

203   was sieved into a fraction 150-180 μm and reduced in the flow of hydrogen (40 mL/min),

204   according to TPR profile, in two steps: 25–250 °C (hold 2 h) and 250–500 °C (hold 2 h) with

205   the temperature ramp of 2 °C/min.

206   Catalytic experiments in a semi-batch mode were performed in the autoclave reactor with a

207   mechanical stirrer (300 mL, Parr Instruments, Figure 1a, Figure S1a) under a continuous flow

208   of hydrogen, 20 mL/min. These experiments were carried out with and without injection of the

209   reactant. In the former case, the following procedure was used: the pre-reduced catalyst (150-

210   180 μ) was loaded into the reactor, the reactor was heated up to the reaction temperature at ca.

211   half of the reaction pressure, and then the pre-heated reactant (100 °C) was injected, the reactor

212   was pressurized and stirring was switched on. In the case of an experiment without injection of

213   the reactant, the pre-reduced catalyst was loaded into the reactor together with the reactant and

214   heated up to the reaction temperature with the heating ramp of 10 °C/min. All batch experiments

215   were carried out at 200 °C (for 1 h) - 250 °C (for 1 h) - 300°C (for 1 h), 30 bar, 1000 rpm with

216   the weight ratio of the reactant-to-catalyst of 25 (i.e. 55 g of the reactant and 2.2 g of the

217   catalyst). The liquid samples were taken directly from the reactor at specific time intervals (1,

218   30, 60, 90, 120, 150, and 180 min). At the outlet line, a separator operating at 0 °C was placed

219   to separate the liquid and gas phases.

220   Catalytic experiments in a continuous mode were performed in a stainless-steel tubular

221   reactor (ID 4.3 mm, L 50 cm, Figure 1b, Figure S1b) operating in a co-current down flow

222   regime. The catalyst (150-180 μm) particles were mixed in the one-to-one volume ratio with

223   inert quartz of the size 250-350 μm, loaded into a reactor and reduced in-situ. The catalytic bed

224 was placed in the slightly lower part of the reactor to ensure that the upper layer (1-1.5 cm) was

225 at the same level as the thermocouple measuring the reactor temperature. The empty space of

226 the reactor upstream and downstream the catalytic bed, separated by quartz wool, was filled

227 with inert quartz of the size 250-350 μm. The liquid reactant was fed to the reactor by Fusion

228 6000-X high-pressure syringe pump (20 mL, 0.0001-51.22 mL/min, up to 108 bar). All

229 continuous experiments were carried out with 0.04 mL/min liquid flow rate of reactant, 15

230 molar excess of hydrogen, at 30 bar of total pressure. The temperature was 250, 270, 300 °C,

231 and the weight of catalyst was 0.1, 0.2, 0.3 g, respectively the liquid residence time 2, 5.5, 11.9

232 min with the weight hour space velocity (WHSV) of 24.4, 12.4, 8.4 $g_{reactant}/g_{catalyst}/h$. At the

233 outlet line, a cooler operating at 1 °C was placed to separate the liquid and gas phases. The

234 liquid samples were taken from the separator at specific time intervals of time-on-stream (TOS

235 1, 15, 45, 60, 90, 120, 180, and 300 min, i.e. the first sample (TOS 1 min) was taken ca. one

236 hour after the start of the liquid flow). A trickling flow regime in the tubular reactor was

237 confirmed by analysis of the flow map considering low gas and liquid flow rates.[15,16]

238
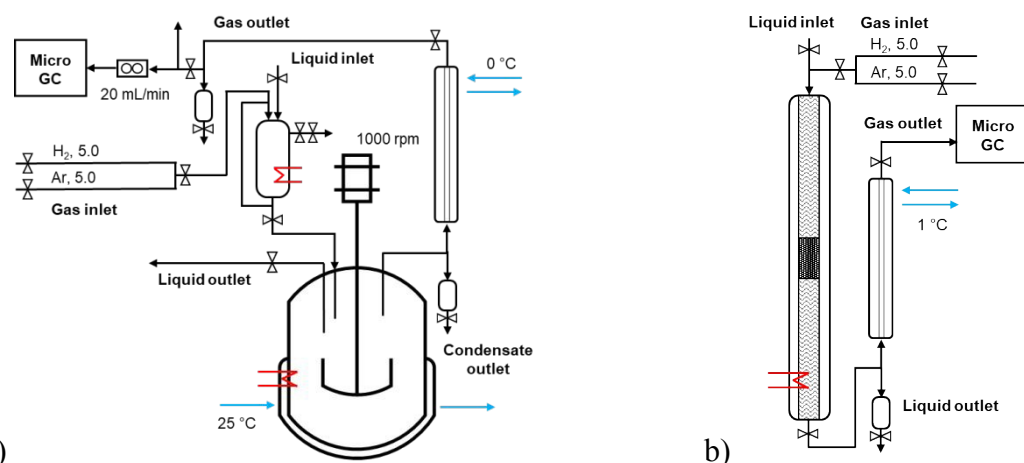
239 *Figure 1. The scheme of the experimental setup: a) batch, b) continuous mode.*

240

241   The liquid samples were analysed by a gas chromatograph (GC) with the FID detector

242 (Agilent 6890N) using DB-1 column (30 m × 250 μm × 0.5 μm). The temperature programme

243   consisted of 4 steps: 60 °C (5 min) – 138 °C (3 °C/min) – 160 °C (1.5 °C/min) – 300 °C (15

244   °C/min, 1 min). Temperature of the detector was 280 °C. The following chemicals were used

245   for calibration of GC analysis: isoeugenol, dihydroeugenol, propylcyclohexane, cyclohexane,

246   hexane, 2,5-dimethylhexane, ethylbenzene. Other products were confirmed with an Agilent

247   GC/MS 6890N/5973 using DB-1 column and the same temperature program. Water content in

248   the samples was analysed by Karl-Fischer titration (736 GP Titrino, Metrohm; Hydranal

249   Composite 2, Fluka). A wide-bore short column GC-FID (PerkinElmer Clarus 500, Shelton,

250   CT, USA) was used to analyze the phenolic dimers. The samples were silylated using N,O-

251   bis(trimethylsilyl)-trifluoroacetamide (BSTFA) as a silylation agent at 60 °C for 1 h. The

252   column parameters were: Agilent HP-1/SIMDIST, ~6 m (length) ×0.530 mm (inner diameter),

253   film thickness 0.15 μm. The flowrate of hydrogen serving as a carrier gas was 7 mL/min. The

254   following temperature program was used: 100 °C (after 0.5 min hold) at a rate of 12 °C/min to

255   340 °C (5 min hold), and with the following injector program: 80 °C (0.1 min hold) at a rate of

256   50 °C/min to 110 °C, and at a rate of 15∘C/min to 330 °C (7 min hold), while the temperature

257   of the detector was maintained at 340 °C. The liquid phase samples were also analyzed by size-

258   exclusion chromatography – high-performance liquid chromatography (SEC–HPLC) technique

259   to detect oligomeric compounds using tetrahydrofuran containing 1% acetic acid as an eluent.

260   The diluted samples were analyzed by a high-performance size exclusion chromatography with

261   an evaporative light scattering detector (HPSEC-ELSD, Shimadzu DGU-405 series modular

262   HPLC, Shimadzu Corporation (Shimadzu, Japan)). SEC–HPLC was equipped with three

263   different columns (2 x Jordi Gel DVB 500A (300 mm x 7.8 mm), Guard column 50 x 7.8 mm).

264   The flow rate of 0.8 ml/min was used with the column oven temperature of 40 °C. The

265   components were detected with an ELSD detector (Sedex-100 LT-ELSD) having the following

266   parameters: 40 °C, air pressure of 3.5 bar and gain 1. The SEC–HPLC system contained the

267   following parts: in-line degasser (Shimadzu DGU-405 degassing unit), the HPLC gradient

268   pump (Shimadzu LG-40D solvent delivery module), an autosampler (Shimadzu SIL-20A HT),

269   the column oven (Shimadzu CTO-10ACvp) and the system controller (Shimadzu CBM-40).

270   The gas samples were analysed online every 15 min by a micro gas chromatograph with

271   TCD detectors (Agilent 6890N) using 4 parallel channels: 1 and 2) 100 °C, MS 5A column (10

272   m × 320 μm × 30 μm) with Plot U pre-column (3 m × 320 μm × 30 μm); 3) 60 °C, Plot Q

273   column (8 m × 320 μm × 10 μm); 4) 90 °C, OV-1 column (14 m × 150 μm × 2 μm). The injector

274   temperature was the same for all channels, 100 °C. The following chemicals were used to

275   calibrate the microGC: hydrogen, ethane, methane, isobutane, n-butane, 1-butene, ethylene,

276   propylene, isobutene, carbon monoxide, carbon dioxide.

2.5   Catalyst regeneration

278   The spent catalyst was regenerated directly in the reactor. After the experiment, the catalyst

279   was kept inside and the reactor was flushed by Ar, 40 mL/min, and cooled down overnight to

280   100 °C. The in-situ regeneration was performed with a step-by-step procedure from 100 °C to

281   400 °C at the heating ramp 2 °C/min, at 5 vol% O_2 in Ar atmosphere, 40 mL/min. The outlet

282   stream was analysed by microGC-TCD removing water upstream the separator. After

283   regeneration procedure, the reactor was flushed by Ar, 40 mL/min, overnight and then re-

284   activated according to the reduction procedure described above.

3 Results and Discussion

3.1   Characterization results of the fresh and spent FeNi/H-Beta-300 catalysts

287   Fresh and spent FeNi/H-Beta-300 catalysts were characterized by a range of physico-

288   chemical methods.

3.1.1 Catalyst particle size distribution

289

290   The fresh Fe-Ni/H-Beta-300 catalyst, after impregnation and calcination, was sieved to a

291   fraction 150-180 μm (Figure S2). This fraction was used for both batch and continuous

292   experiments. The particle size distribution of the sieved fraction for the fresh and spent

293   catalysts, from the batch and continuous mode experiments with isoeugenol as a reactant was

294   determined by laser diffraction. The results showed that 50% of the fresh catalyst particles have

295   a size of 177 μm or smaller, while for the spent catalysts it was slightly larger, D_{v50} of 195 μm

296   (Figure S2b, Table 4). This could be related to agglomeration of the small particles due to

297   adsorption of heavy compounds on the catalyst (coke).

3.1.2 Surface morphology

298

299   The surface morphology of the fresh FeNi/H-Beta-300 catalyst is shown on the scanning

300   electron microscope (SEM), back-scattered electron (BSE) images, and energy dispersive X-

301   ray (EDX) mapping analysis in Figure S3. The presence of large spherical agglomerated

302   particles of a bimetallic catalyst with an average size of 300 nm is in line with the morphology

303   results and the average particle size of the pristine H-Beta-300 zeolite.[17] SEM in the back-

304   scattered electron mode revealed large particles in the range of 80-950 nm with the similar

305   average, 330 nm. According to EDX spot and EDX mapping analysis (Figure S3b), the

306   composition of the highlighted particles comprised both Fe and Ni in different ratios. This result

307   indicates that the catalyst contains metal particles with very different compositions, indicating

308   its very heterogeneous character.

3.1.3 Elemental analysis

309

310   Elemental analysis of the fresh FeNi/H-Beta-300 catalyst (12 mm^2) revealed the ca. half

311   value of the SiO_2/Al_2O_3 molar ratio, i.e. 159, compared to the nominal one indicated by the

312   manufacturer (i.e. the last number in the zeolite name). This is in line with the literature[17]

313   reporting data for pristine zeolites. The metal concentrations, determined by either EDX and

314   ICP-OES, were close to the nominal loading with the molar metals ratio of 1 (Table S1). After

315   the batch experiment with isoeugenol, leaching of metal was ca. 17% from the spent catalyst

316   determined by ICP-OES, while the molar metals ratio remained the same (Table S1).

317   *3.1.4 Metal particle sizes*

318   The metal particle sizes were determined by TEM (Table 1, Figure S4). However, it should

319   be noted that in TEM analysis, the contrast arises from differences in electron scattering

320   between the sample and the surrounding medium. Both iron and nickel have similar atomic

321   numbers, resulting in a very limited elemental contrast between them. This lack of contrast, and

322   the fact that iron and nickel have also similar crystal structures and atomic radii, further hampers

323   ability to distinguish between Fe and Ni nanoparticles. In addition, bimetallic catalysts often

324   involve formation of alloys and clusters containing Ni and Fe with different compositions (as

325   was presented above by EDX). Therefore, Fe and Ni in the catalysts could not be separated

326   from each other in the current work and the median of all metal particles is expressed as d_{NiFe}

327   (Table 1, Figure S4).

328   Worth noting is that, for most catalysts, the histogram of FeNi particle size clearly revealed

329   two maxima. For this reason, the fitting of Kernel Smooth distribution curves by the Gauss

330   function was also used (Figure 2). Acknowledging all limitations of the applied approach, the

331   results were compared with Fe_2O_3[18] and the monometallic Fe (5-5.5 nm) and monometallic Ni

332   (18.1-19.2 nm) catalysts on another zeolitic support (H-Y-5.1) used in the previous work.[12]

333   Both ranges are in line with the maxima for fresh and spent bimetallic FeNi/H-Beta-300

334   catalysts used in the current work. To be specific, the first maximum with the median particle

335   size of 5-7 nm could hypothetically correspond to Fe and particles rich in Fe (d_{Fe}^f) assuming the

336   same size of iron clusters formed after deposition on beta and Y zeolites, and the second

Sustainable Energy & Fuels Accepted Manuscript

337 maximum with a median particle size of 15-22 nm reflects subsequently Ni and particles rich

338 in Ni (d_{Ni}^f).

339   Based on the comparison of the median particle size of both fresh and spent catalysts no

340 sintering of the metal particles in hydrodeoxygenation of isoeugenol or dihydroeugenol in either

341 batch (3 h) or continuous reactor (5 h) at 250-300 °C and 30 bar of total pressure could be

342 confirmed. Moreover, neither a decrease in the particle size was observed (Table 1, entry 1),

343 although slight leaching was detected by ICP-OES. (Table S1).

344   Metal dispersion in the fresh and spent catalysts calculated from the non-fitted and fitted

345 median particle sizes of FeNi was relatively close to each other, D_{FeNi} of 7-18% and D_{FeNi}^f of

346 11-16%, respectively (Table 1, Figure S4). It should be also mentioned that the differences in

347 metal particle size of catalysts could be related to the alloy formation. Metals dispersion was

348 calculated according to:

$$D_{FeNi} = (x_{Fe} \cdot 116 + x_{Ni} \cdot 101)/d_{FeNi} \tag{1}$$

$$D_{FeNi}^f = x_{Fe} \cdot D_{Fe}^f + x_{Ni} \cdot D_{Ni}^f \tag{2}$$

349   where x_{Fe}, x_{Ni} is the metal molar fraction of the fresh catalyst determined from ICP-OES,

350 D_{Fe}^f, D_{Ni}^f is dispersion of single metals calculated using the formula described by Sholten et

351 al.[19] assuming spherical shapes of metals, giving $D_{Fe} = 116/d_{Fe}^f$, $D_{Ni} = 101/d_{Ni}^f$,[19-21] and d_{Fe}^f,

352 d_{Ni}^f is the median particle size of single metals obtained from TEM (in nm) by fitting of Kernel

353 Smooth distribution curves by the Gauss function.

354 *Table 1. Median metals particle sizes and metals dispersion determined by TEM analysis of the fresh and spent*
355 *catalysts. Legend: DHE – dihydroeugenol, IE – isoeugenol, B – batch, C – continuous mode, d – median particle*
356 *size, f – metals dispersion based on particle size determined by TEM and molar metals ratio of fresh catalyst*
357 *determined by ICP-OES. D^f – metals dispersion based on particle size fitting and molar metals ratio of fresh*
358 *catalyst determined by ICP-OES.*

Entry	Catalyst	DHE/IE	B/C	Conditions	d_{FeNi}	D_{FeNi}	d_{Fe}^f	d_{Ni}^f	D_{Fe}^f	D_{Ni}^f	D_{FeNi}^f
					nm	*%*	*nm*	*nm*	*%*	*%*	*%*
0a	fresh, calcined	-	-	-	7	16	5	16	24	6	15
0b	fresh, reduced	-	-	-	8	14	6	20	20	5	13
1	spent	IE	B	250-300 °C, 2.2g	8	14	7	-	18	-	-

2	spent	DHE	B	250-300 °C, 2.2g	15	7	6	20	18	5	12
3	spent	DHE	B*	250-300 °C, 2.2g	11	10	7	22	18	5	11
4	spent	IE	C	300 °C, 0.2g	9	12	5	21	22	5	13
5	spent	IE	C	300 °C, 0.3g	8	14	6	-	18	-	-
6	spent	IE	C	275 °C, 0.3g	6	18	5	18	26	5	16
7	spent	IE	C	250 °C, 0.3g	8	14	5	-	23	-	-
8	spent	DHE**	C	300 °C, 0.1g	7	16	6	15	20	7	13
9	spent	DHE**	C	300 °C, 0.3g	15	7	6	18	20	6	13

359 * with injection of the reactant on the preheated reduced catalyst, ** two runs, f – fitting of Kernel Smooth
360 distribution curves by the Gauss function in Origin.
361
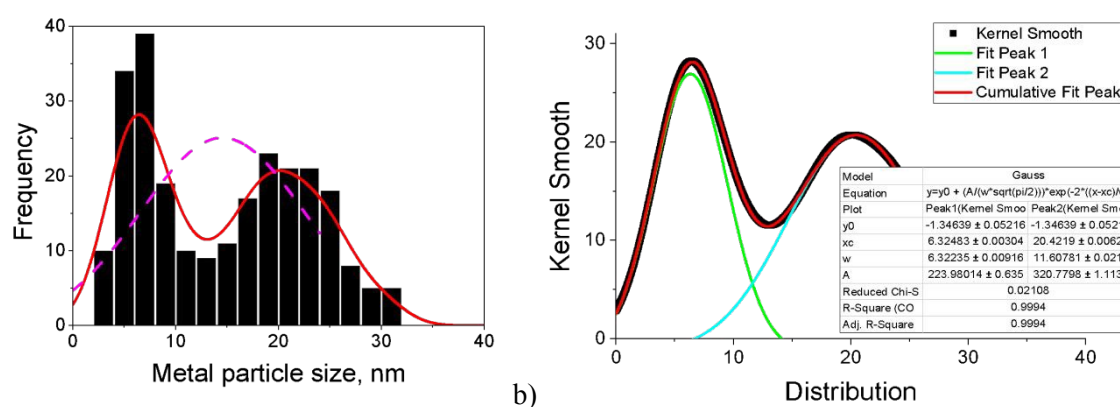
362 *Figure 2. a) histogram of FeNi particle size and b) fitting curves of Kernel Smooth distribution for the spent*
363 *catalyst after dihydrogenol hydrodeoxygenation in the batch reactor (Table 1, entry 2).*
364

365 *3.1.5 Brønsted and Lewis acid sites, and metal-to-acid site ratio*

366   Brønsted and Lewis acidity (Table 2) was determined by FTIR with pyridine as a probe

367 molecule. The total acidity of the catalyst remained moderate, 104 μmol/g, while the ratio of

368 the Brønsted and Lewis acid sites (B/L) significantly decreased from 6 to 0.8, after

369 impregnation of metals. In line with the literature,[12, 22, 23] introduction of Fe led to a decrease of

370 strong Brønsted acid sites which was explained by the interaction of iron species with the acidic

371 sites on the zeolite surface, involving formation of metal clusters that can occupy or block the

372 active sites, the coordination of iron species with oxygen atoms or hydroxyl groups, and

373 modification of the electronic structure of the zeolite surface. Introduction of both unreduced

374 Fe and Ni elevated weak and medium Lewis acid sites.

375 After isoeugenol hydrodeoxygenation in the batch reactor a slight decrease of weak and

376 medium Lewis acid sites from 57 to 31 μmol/g was noticed which led to higher B/L. This

377 decrease could be related to Fe and/or Ni leaching (Table S1) as wells as coke formation during

378 reaction (Table 4) which can adsorb onto the surface of the catalyst, potentially masking or

379 blocking the Lewis acid sites. The metal-to-acid site ratio slightly increased after isoeugenol

380 hydrodeoxygenation in the batch reactor from 15.5 to 17.3 (Table 2). While Fe and/or Ni

381 leaching might cause a reduction in the total metal content on the catalyst surface, it does not

382 necessarily imply a direct correlation with the decrease in Lewis acid sites. In fact, the increase

383 in the metal-to-acid site ratio indicates that the metal content, relative to the remaining acid

384 sites, has increased. This could be due to a preferential loss of acid sites or a redistribution of

385 the metal species on the catalyst surface. FTIR-pyridine spectra are provided in the supporting

386 information in Figure S5.

387

388 *Table 2. Brønsted and Lewis acid sites of the support, fresh and spent FeNi/H-Beta-300 catalysts and their metals-*
389 *to-acid site ratio (n_{FeNi}/n_{AS}). Legend: IE – isoeugenol, BAS – Brønsted acid sites, LAS – Lewis acid sites, TAS –*
390 *total acid sites, B/L – ratio of the Brønsted and Lewis acid sites, s (strong acid sites, data at 450 °C), m (medium*
391 *acid sites, data at 350 °C minus data at 450 °C), and w (weak acid sites, data at 250 °C minus data at 350 °C).*

| Catalyst	TAS	BAS	LAS	BAS			LAS			B/L	n_{FeNi}/n_{AS}
-		μmol/g		w	m	s	w	m	s	-	mol/mol
H-Beta-300	77	66	11	16	28	23	5	2	3	6.0	-
5-5 wt% Fe-Ni/H-Beta-300	104	47	57	24	23	0	34	23	0	0.8	15.5
spent catalyst (batch, IE)	77	46	31	18	28	0	16	15	0	1.5	17.3

392

393 *3.1.6 Phase identification and the metal valence*

394 The XRD pattern of the fresh catalyst is displayed in Figure 3 together with unfitted crystal

395 models for Beta polymorph A, Fe and Ni, showing that the zeolite structure remained the same

396 after metals impregnation. All the phases can be identified from the data. However, the Ni phase

397 seems to be under a considerable uniform strain since the lattice parameters deviate

398   considerably from the literature values. Identification is therefore based on the assumption that

399   no additional phases are present in the sample. Ni (Fm-3m) lattice system is a common crystal

400   structure for various metals (for example Cu, Co), which can lead to misinterpretation of the

401   data.

402
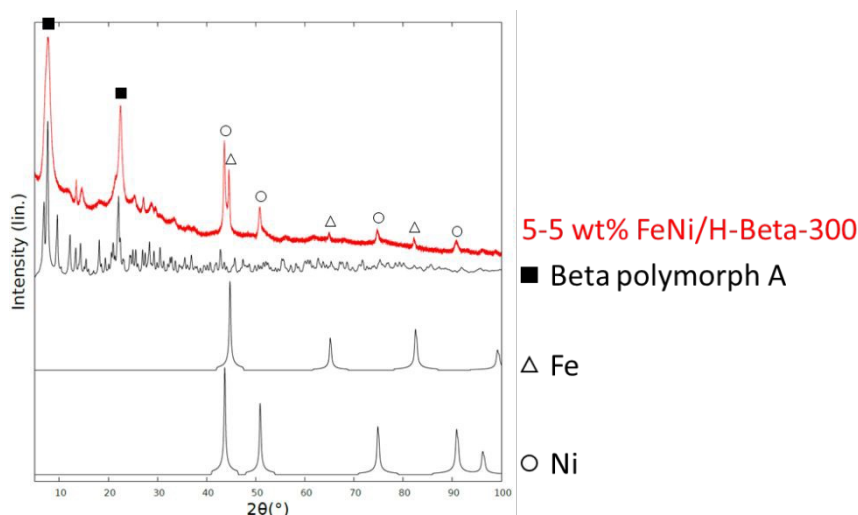
403
404   *Figure 3. XRD pattern of the fresh catalyst.*
405

406   According to Mössbauer spectroscopy (Figure 4a), the fresh 5-5 wt% Fe-Ni/H-Beta-300

407   catalyst at 22 °C is dominated by two sextets related to metallic Fe (red is more typical, blue is

408   broadened and has a smaller field probably due to interactions with nickel). Cyan and brown

409   doublets in Figure 4a represent a small amount of Fe^{3+} or possible superparamagnetic Fe and

410   marginal amounts of paramagnetic Fe^{2+}, respectively. It should be mentioned that significant

411   differences in results of the Fe valence state composition in the bulk and Mössbauer parameters

412   (Table 3) were obtained for 5-5 wt% Fe-Ni/H-Y-5.1 synthesized and reduced by the same

413   method (cit.[12], Figure 4b) as in the current work. While the metallic form of Fe dominated

414   (93%) for Fe-Ni catalyst supported on mildly acidic H-Beta-300, in the case of a more acidic

415   H-Y-5.1 with the total acidity of the pristine support of 172 μmol/g comprising 154 μmol/g

416   Brønsted acid sites,[12] it was predominantly Fe^{3+} (52%). Such differences could be explained by

417   different metal-metal and metal-support interactions in these catalysts.

418

a)   b)
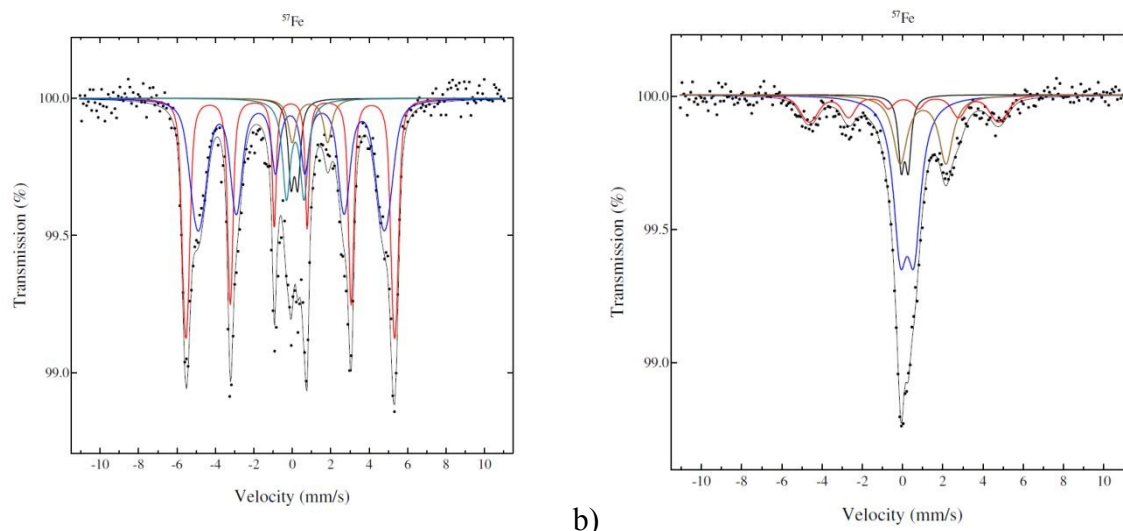
419   *Figure 4. Mössbauer spectra of the fresh catalyst: a) 5-5 wt% Fe-Ni/H-Beta-300, legend: metallic and magnetic*
420   *Fe (red, blue), Fe^{2+} (brown), Fe^{3+} (cyan), Fe impurity in the detector (black); b) 5-5 wt% Fe-Ni/H-Y-5.1 [12], legend:*
421   *metallic and magnetic Fe (red), Fe^{2+} (beige), Fe^{3+} (blue), Fe impurity in the detector (black).*

422

423   *Table 3. The valence state of Fe in the bulk of catalysts determined by Mössbauer spectroscopy, and Mössbauer*
424   *parameters. Legend: δ - isomer shift in mm/s, ΔEQ – quadrupole splitting in mm/s, B – internal magnetic hyperfine*
425   *field in T, μ_{Fe} - magnetic moment of iron, assuming spin-only contribution to the field.*

| Catalyst	Fe^0	Fe^{2+}	*Fe^{3+}	$δ_{Fe0}$	$δ_{Fe2+}$	$δ^*_{Fe3+}$	$ΔEQ_{Fe2+}$	$ΔEQ^*_{Fe3+}$	B_{Fe0}	μ_{Fe}
5-5 wt% Fe-Ni/H-Beta-300	93	2	5	0.03	1.04	0.28	1.85	0.92	33	4.0
5-5 wt% Fe-Ni/H-Y-5.1**	22	26	52	0.18	1.14	0.35	2.27	0.69	29	3.6

426   * predominantly Fe^{3+}, ** from the literature [12]

427

428   XAS was used to investigate the local structure around Fe and Ni atoms in the as-received

429   (calcined) and reduced fresh and spent FeNi/H-Beta-300 (FeNi/β, batch, IE, Table S2) catalysts.

430   It is noteworthy that the catalysts were reduced directly in in-situ cells with a plug-flow

431   geometry according to the protocol used for catalytic testing, then cooled down and either

432   directly measured in flowing H_2 or sealed in the cell under H_2 and measured later without a

433   need for any passivation or exposure to air. XANES and Fourier transformed (FT) EXAFS

434   spectra of the as received catalysts (fresh after calcination, spent after exposure to air) are

435   depicted in Figure 5 alongside spectra of the most relevant oxidized reference compounds. The

436   position and the shape of pre-edge and edge features in the Fe K XAS spectra (Figure 5a,c)

437   correspond to γ-Fe$_2$O$_3$ nanoparticles (nanosizing effect seen from lower scattering intensity on

438   the 2nd and further shells compared to the reference spectrum, Figure 5c). This is in line with

439   the literature[12] attributing the initial presence of Fe(III) to the used Fe(NO$_3$)$_3 \cdot$9H$_2$O precursor.

440   Qualitatively, the iron oxide nanoparticle size decreased after activation, the catalytic test and

441   a subsequent exposure to air. Ni K XAS spectra (Figure 5b,d) demonstrate the same trend: bulk-

442   like NiO in the fresh calcined sample with a somewhat more dispersed oxide in the spent

443   catalyst (Figure 5d). This trend was not clearly demonstrated by TEM (Table 1, entry 1).

444

a)

b)
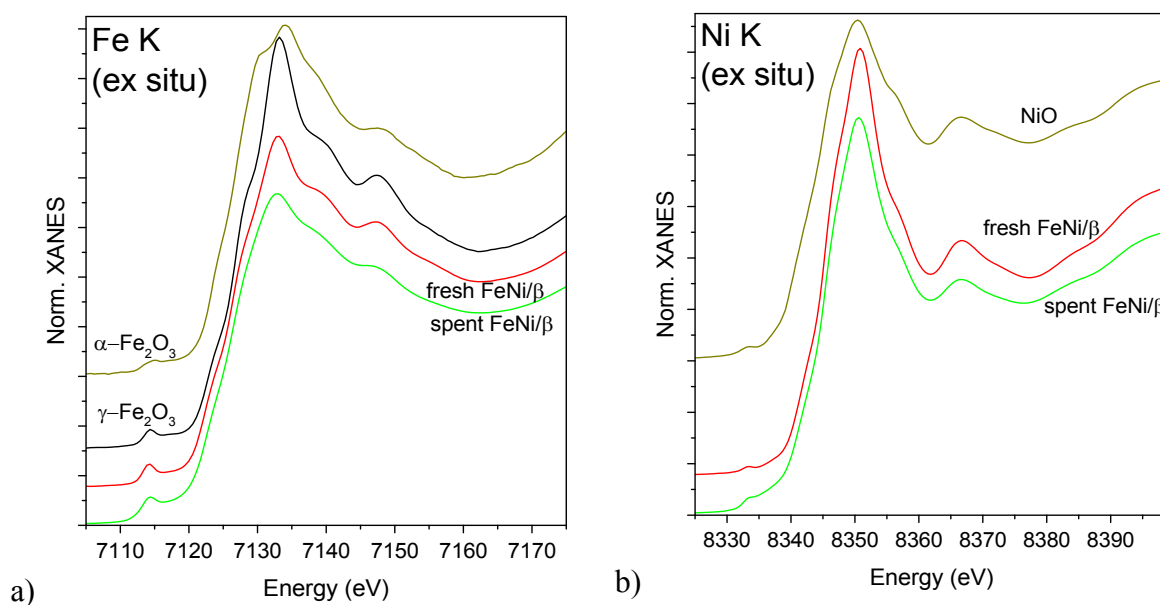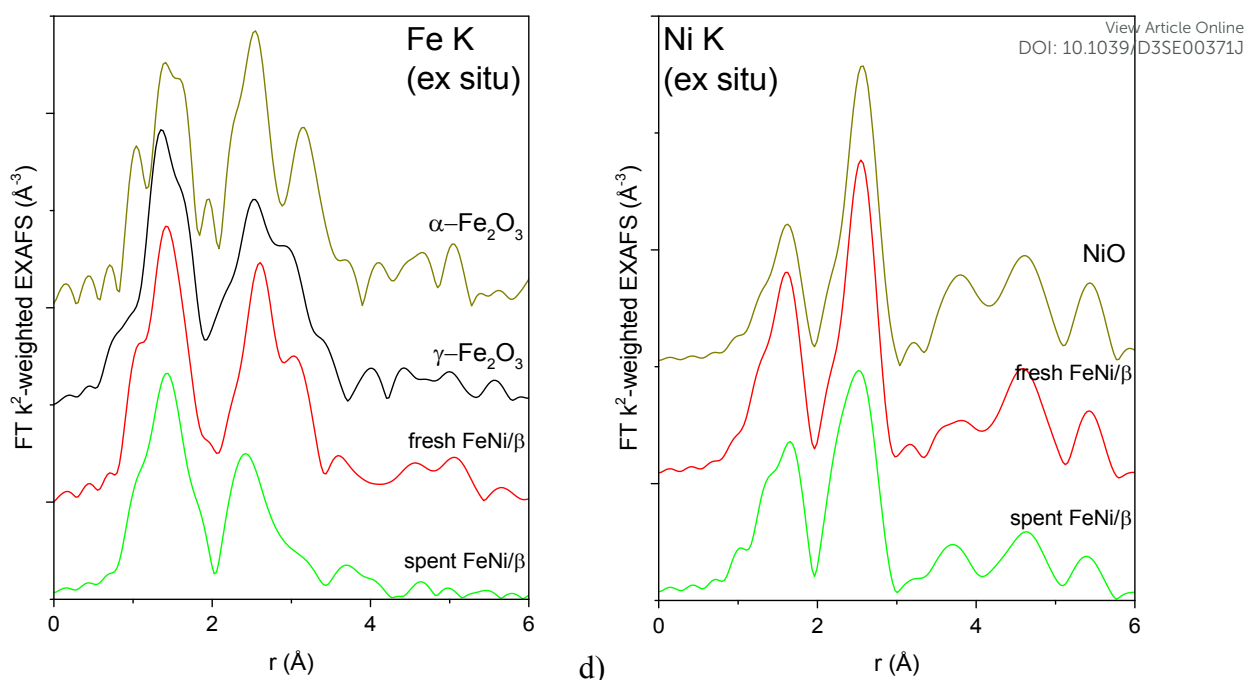
Figure 5. Normalized XANES (a,b) and Fourier transformed EXAFS (c,d) spectra of the calcined and exposed to air spent catalyst and relevant reference compounds measured at Fe K (a,c) and Ni K (b,d) edges. EXAFS spectra are not corrected for the phase shift.

XAS spectra of the reduced catalysts are shown in Figure 6. Edge positions in the XANES spectra confirm the reduced state of both Fe and Ni in all studied bimetallic catalysts (Figure 6a,b). Bulk Fe and Ni metals crystallize in different structures under ambient conditions: bcc (Im-3m) in the case of Fe and fcc (Fm-3m) structure for Ni. The different crystal structures result in very different XANES spectra for the respective individual metals (Figure 6a,b). The fcc structure around Ni atoms is preserved for both samples, although the Ni K XANES spectrum of the spent catalyst displays a white line with a higher intensity and shape, possibly due to partial oxidation (Figure 6b). This partial oxidation may happen due to exposure of the sample to air during transportation to the synchrotron and therefore O-related features will not be used for drawing conclusions. On the other hand, the peaks at 8357 and 8382 eV are due to the metallic structure. These peaks are shifted to lower energies in the case of both bimetallic samples with the shift being less pronounced for the spent catalyst. This shift may indicate alloying with Fe, and subsequently different shifts reflect different degrees of alloying (i.e.

462   partial dealloying after catalysis and exposure to air). All Ni K EXAFS spectra (Figure 6d)

463   unequivocally confirm the fcc Ni structure.

464   Fe K XAS spectra (Figure 6a,c) of the reduced fresh and spent catalysts are markedly

465   different from bcc Fe and rather suggest the fcc structure as in the case of Ni which signifies

466   FeNi alloy formation.

467
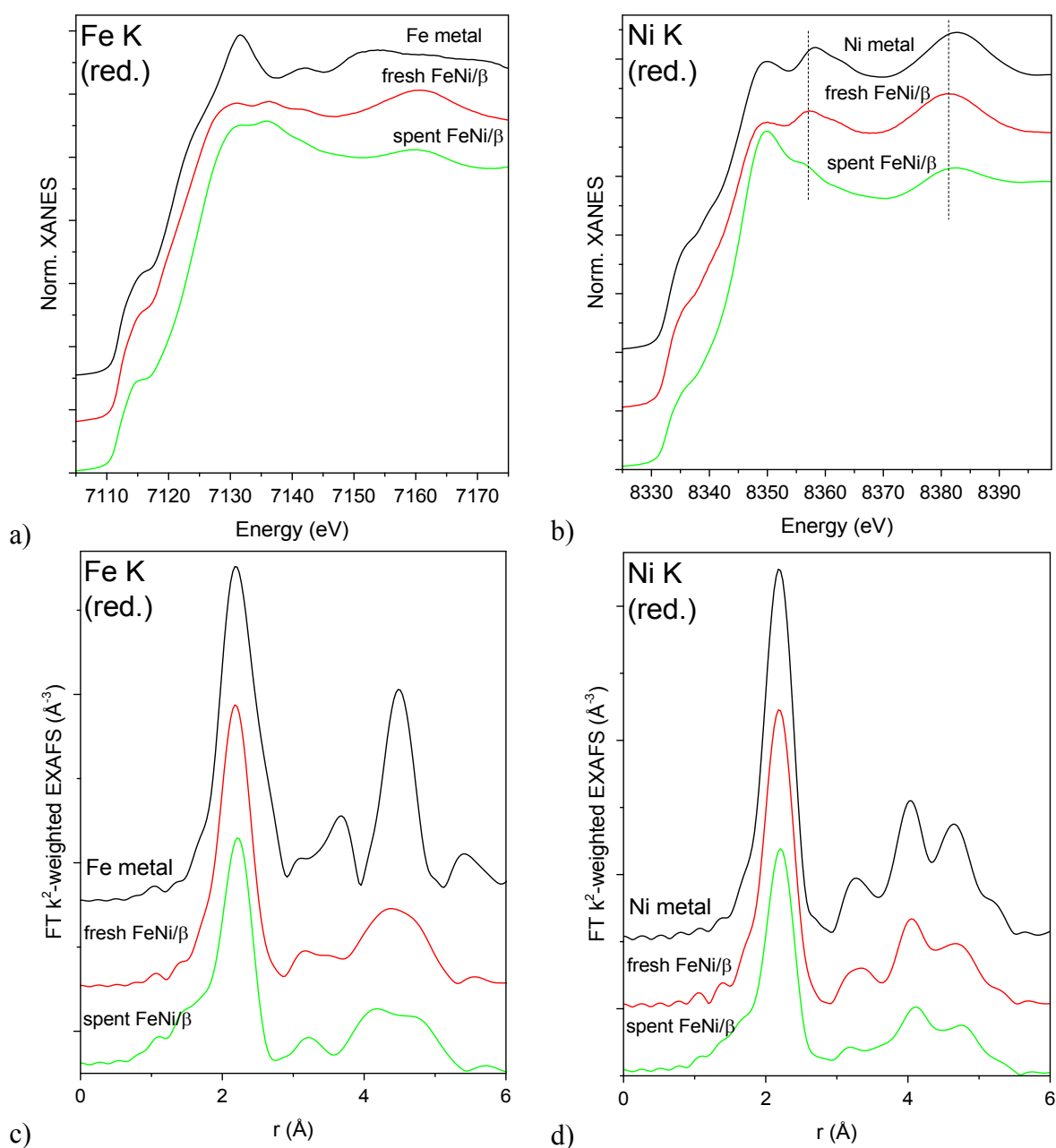
468 *Figure 6. Normalized XANES (a,b) and Fourier transformed EXAFS (c,d) spectra of reduced fresh and re-reduced*
469 *spent catalyst and the respective bulk metals (5 μm thick foils) measured at Fe K (a,c) and Ni K (b,d) edges. EXAFS*
470 *spectra are not corrected for the phase shift.*

471

472   The first shell analysis was performed on Fe K and Ni K EXAFS spectra of the reduced

473   samples to identify structural parameters such as the coordination number and interatomic

474   distances (Table S2, Figure S6, Figure S7, Figure S8). Due to similar scattering factors of Fe

475   and Ni, EXAFS cannot reliably distinguish between these two types of the nearest neighbours.

476   The obtained structural parameters point at fcc structures around both Fe and Ni atoms in both

477   samples. Coordination numbers around 11 in the fresh reduced FeNi sample correspond to

478   rather large, on the order of 3-10 nm (with large error bars due to uncertainty in CN

479   determination and asymptotic behaviour of the model)[24] fcc FeNi nanoparticles. The same CN

480   around Ni and Fe suggest random distribution of both metals in the alloy. Somewhat longer Fe-

481   M mean interatomic distance in the spectrum of the spent and rereduced FeNi/H-Beta-300

482   (FeNi/β) may signify a contribution from the bcc Fe structure (i.e. partial dealloying), while

483   lower average coordination numbers around both Fe and Ni (ca. 9.3 at an average) stem from a

484   smaller mean metal particle size of 1.5-2 nm. Significantly smaller particle sizes determined by

485   EXAFS, compared to TEM, are probably related to the EXAFS sensitivity to single coherently

486   scattering domains and TEM observing their aggregates and agglomerates.

487   *3.1.7 Reducibility*

488   Reducibility of FeNi/H-Beta-300 is shown by the TPR profile in Figure 7a. In comparison,

489   the TPR profile of FeNi/H-Y-5.1 (Figure 7b, cit.[12]) prepared by the same method with the same

490   nominal metals loading and reduced under the same conditions is also presented in the same

491   Figure. Such comparison clearly shows different interactions in FeNi catalyst supported on

492   different supports, which was already indicated by the results from Mössbauer spectroscopy

493   reported above. The first temperature maximum in TPR for hydrogen consumption was

494   obtained at a comparable temperature of 390-395 °C, which corresponds to the reduction of

495   Fe(III) to Fe(II).[12,25] This is in line with XANES spectra of the fresh catalyst (Figure 5a)

496   showing initial presence of Fe(III) in the form of maghemite (γ-Fe_2O_3) originating from the

497    $Fe(NO_3)_3 \cdot 9H_2O$ precursor. The second maximum was delayed by 90 °C for 5-5 wt% Fe-Ni/H-

498   Beta-300 catalyst indicating stronger binding of Ni-species with Beta zeolite compared to H-

499   Y-5.1.[12,26-28] However, it should be mentioned that the relative peak area was the same for both

500   catalysts between 100-800 °C, whereas, the relative peak area bellow the reduction temperature,

501   100-500 °C was slightly higher, 1.3-fold, for 5-5 wt% Fe-Ni/H-Y-5.1.

502
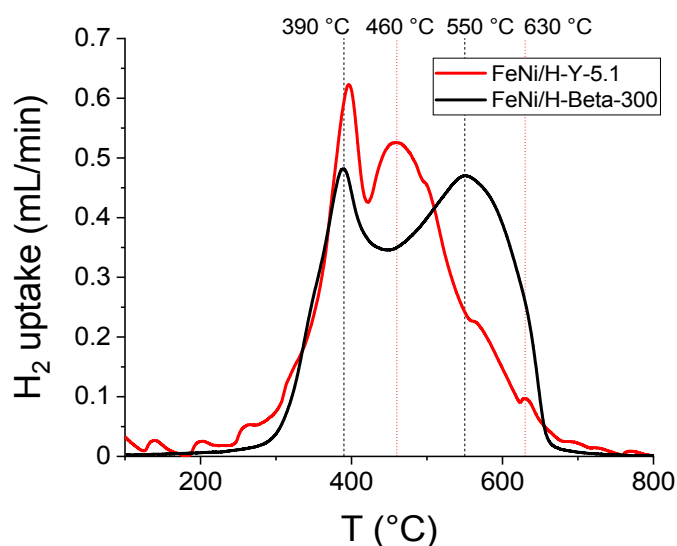
503
504   *Figure 7. H_2-TPR profiles of the fresh catalyst: 5-5 wt% Fe-Ni/H-Y-5.1 (data from cit.[12]) and 5-5 wt% Fe-Ni/H-*
505   *Beta-300.*

506

507   *3.1.8 Textural properties and coke analysis*

508   The specific surface area for the fresh catalyst was 516 m^2/g with 0.26 cm^3/g of the total pore

509   volume comprising 81 vol% micropores (< 2 nm) (Table 4, entry 0). After the reaction, a

510   significant drop in both the specific surface area and pore volume of the catalyst was observed

511   (Table 4, entries 1-9). From the pore size distribution of the spent catalyst it can be concluded

512   that both micro and mesopores were clogged relatively equally (Figure 8). The most dramatic

513   decrease in the textural properties such as the surface area according to the Dubinin-

514   Radushkevich method (ca 99%) was observed for the catalyst used in the continuous mode with

515   isoeugenol as the reactant, especially at HDO temperature of 300 °C (Table 4, entries 4,5).

516   In-situ regeneration of the spent catalyst was simulated by an O_2-TPO-TCD-MS

517   measurement performed at the same conditions over the catalyst from the batch experiment of

518   isoeugenol hydrodeoxygenation (Table 4, entry 1a). The textural properties of the regenerated

519   catalyst obtained by this procedure clearly demonstrated the success of removing coke at 100-

520   400 °C. The mesoporosity was fully regenerated while the specific surface area and

521   microporosity of the regenerated catalyst achieved 80% of values compared to the fresh catalyst

522   (Figure 8, Table 4, entry 1b). In the case of the catalyst regeneration by burning coke up to 900

523   °C (O_2-TPO-TCD-MS, 100-900 °C, 5 °C/min), the comparable micropore volume was

524   recovered compared to a similar treatment to a much lower temperature (O_2-TPO-TCD-MS,

525   100-400 °C, 2 °C/min). The specific surface area and total pore volume were comparable, i.e.

526   ca 80% of the original value for the fresh catalyst.

527   TEM images of the catalysts regenerated at 400 °C and 900 °C are shown in Figure S9. The

528   metal particle size after regeneration at 400 °C varies in the range of 10 - 25 nm indicating that

529   metal particles are not sintered due to strong interactions between the metal and acidic zeolite.

530   However, sintering clearly occurred after catalyst regeneration at 900 °C, when the metal

531   particles of 15 – 60 nm were observed in the images (Figure S9c,d). These results together with

532   surface area measurements demonstrate that it is not possible to fully regenerate the catalyst

533   even at a high temperature, because the surface area could not be fully recovered and metal

534   sintering occurred.

535

536   *Table 4. Textural properties of the fresh and spent catalysts and the mass of heavy compounds adsorbed on the*
537   *catalyst (coke) after the reaction determined by TGA (100-800 °C), CHNS or TPO (100-900 °C) analysis. Legend:*

B – batch, C – continuous mode, DHE – dihydroeugenol, IE – isoeugenol, T – reaction temperature, m_{cat} – weight of catalyst, D_v – particle size (decimal fraction), S_{D-R} – the specific surface area calculated by Dubinin-Radushkevich method, V – the total pore volume calculated by non-local density functional (DFT), V_μ - the micropore volume (DFT), V_m – the mesopore volume (DFT), R_c – the rate of coke formation (µg of coke/mg of catalyst/h), m_c – weight of coke in the spent catalyst determined by TGA.

Entry	Catalyst	B/C	DHE/IE	T	m_{cat}	S_{D-R}	V	$V\mu$	$V\mu/Vm$	R_c	$m_{c,TGA}$	$m_{c,CHNS}$	$m_{c,TPO}$
				°C	g	m²/g	cm³/g	vol%	-	µg/mg/h	wt%	wt%	wt%
0	fresh	-	-	-	-	516	0.26	81	4.2	-	0	0	0
1a	spent	B	IE	250-300	2.2	202	0.12	66	1.9	27.0	8.1	8.2	9.5
1b	regenerated 1a cat. (TPO 100-400 °C)					415	0.23	72	2.6	-	3.2	-	-
1c	regenerated 1a cat. (TPO 100-900 °C)					413	0.21	77	3.3	-	-	-	-
2	spent	B	DHE	250-300	2.2	178	0.16	39	0.6	31.0	9.3	-	-
3	spent	B*	DHE	250-300	2.2	204	0.13	66	1.9	25.0	7.5	-	-
4	spent	C	IE	300	0.2	4	0.01	14	0.2	36.2	18.1	-	-
5	spent	C	IE	300	0.3	5	0.01	11	0.1	37.0	18.5	-	-
6	spent	C	IE	275	0.3	19	0.17	1	0.01	26.2	13.1	-	-
7	spent	C	IE	250	0.3	117	0.11	41	0.7	24.2	12.1	-	-
8	spent	C	DHE**	300	0.1	163	0.09	75	2.9	12.2	6.1	-	-
9	spent	C	DHE**	300	0.3	143	0.09	61	1.6	21.8	10.9	-	9.2

* with injection of reactant on the preheated reduced catalyst, ** two runs
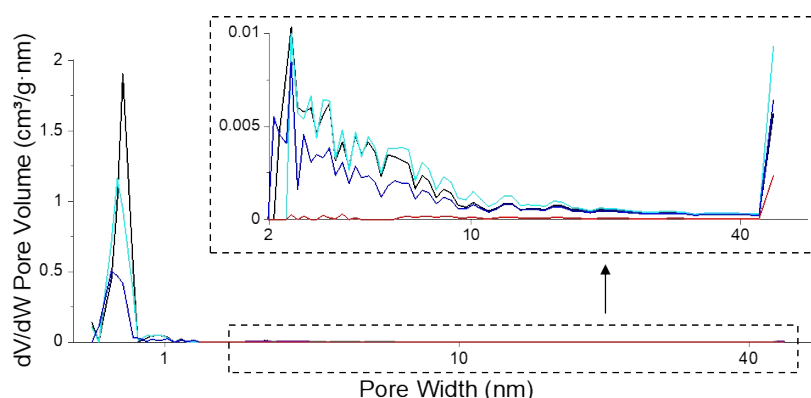
Figure 8. Pore size distribution of fresh (black), spent catalysts after isoeugenol hydrodeoxygenation in the batch reactor from (blue, Table 4, entry 1a) and in the continuous reactor (red, Table 4, entry 5) and regenerated catalyst (cyan, Table 4, entry 1b).

It was also revealed that the specific surface area of the spent FeNi/H-Beta-300 catalysts, tested at different conditions, linearly decreased with the increasing amounts of coke determined by TGA analysis (6-19 wt%, Figure 9, Table 4). This is valid for all catalysts including in-situ regenerated catalyst. In other words, the formation of one weight percent of

554   coke in the catalyst led to a decrease in the specific surface area of approx. 12.7%; i.e. a 50%

555   decrease in the specific surface area of the catalyst corresponds to ca 7.7 wt% coke formation.

556   This is the opposite trend that was obtained over FeNi/H-Y-5.1 catalyst with different ratio of

557   metals, tested in co-processing of n-hexadecane with lignin derived isoeugenol.[11] It could be

558   related to catalyst composition but also to the different feedstock.
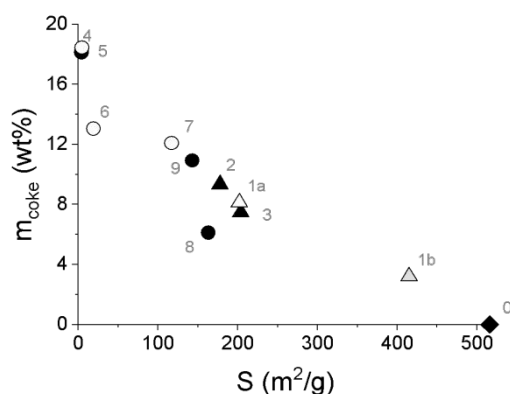
559
560   *Figure 9. Amount of coke determined by TGA as a function of the catalyst specific surface area. Legend: fresh*
561   *catalyst (diamond), spent catalyst from the batch experiment (triangle), spent catalyst from the continuous*
562   *experiments (circle), spent catalyst from IE HDO (open symbols) and spent catalyst from DHE HDO (black*
563   *symbols), regenerated catalyst (grey symbol, in-situ regeneration of the spent catalyst simulated by O_2-TPO).*
564   *Notation is the same as in Table 4.*
565

566   According to the heat release, two maxima were obtained in 355-380 °C and 470-480 °C

567   temperature regions for all the spent catalysts used in IE HDO (Figure S10a) and DHE HDO

568   (Figure S10b). This is in line with filamentous type coke formation (400-550 °C) observed also

569   over Ni-UpGraded Slug Oxides,[29] and FeNi/H-Y-5.1.[12] Sánchez-Sánchez et al.[30] reported that

570   the oxidation of filamentous coke coupled with Ni particles occurs in the temperature range

571   between 300 and 530 °C, while the oxidation of carbonaceous deposits with various degrees of

572   graphitization occurs above 530 °C.

573   Similar results as from TGA were obtained from the TPO analysis (Figure S11), i.e. two

574   maxima of carbon oxidation at 370 °C and 485 °C for the spent catalyst, used in IE HDO in the

575   batch reactor. The weight ratio of CO-to-CO_2 formation was 18/82 (wt%), i.e. 0.21. For the

Sustainable Energy & Fuels

576   same catalyst (Table 4, entry 1a), 9.5 wt%, 8.1 wt%, 8.2 wt% coke was determined by TPO

577   (100-900 °C), TGA (100-800 °C), and CHNS (950 °C), respectively. Furthermore, CHNS

578   analysis also revealed the molar H/C ratio of 1.8, pointing on the presence of aliphatic species

579   with a mean value of molar H/C ratio ca. 1.7 (1.4 < H/C < 2.0), having higher H/C ratios than

580   aromatic compounds (ca. 0.6).[31]

581   An analogous result was also obtained by identification of the extracted soluble coke species

582   using GC-MS. The extracted soluble coke from the spent catalysts, used in the batch mode

583   experiments without injection of the reactant on the preheated fresh catalyst, showed a broad

584   range of predominantly aliphatic coke (primary compounds: C10-C18 straight-chain alkanes)

585   and a low amount of aromatics (primary component: dimethylethyl benzene) (Figure S12).

586   Analogous results were obtained from the co-processing of n-hexadecane with lignin derived

587   isoeugenol performed also in the batch mode.[11] On the other hand, the results from the batch

588   mode with injection (Figure S12) and the continuous mode (Figure S13), obtained in the current

589   work in IE HDO and DHE HDO, revealed selective coke formation of n-C16 with minor

590   amounts of n-C12 and i-C16 straight-chain alkanes. These results can be attributed to the

591   specific reaction conditions in the applied experimental setups determining the selective

592   formation and composition of the coke species. In the case of the batch experiment without the

593   injection, the catalyst was exposed to the reactant during the heating period without stirring.

594   Absence of stirring may have led to the strong adsorption of the reactant on the catalyst surface.

595   The combination of strong adsorption and a sufficiently long contact time in the batch

596   experiment could have been the reason for ormation of a wide range of coke species.

597   For the coke species analysis on the surface of the spent catalyst, also Raman spectroscopy

598   with different wavelengths (355 nm, 514 nm, 532 nm, 633 nm, 785 nm and 1064 nm) has been

599   employed. This technique was previously applied for metal-free ZSM-5, USY zeolites (UV

Sustainable Energy & Fuels Accepted Manuscript

600   Raman, cit.[32]), Pt-Sn/Al$_2$O$_3$ (514 nm, cit.[33]), Mn$_3$O$_4$ (785 nm, cit.[34]), Pt-Re/γ-Al$_2$O$_3$ (785 nm,

601   cit.[35]), Au nanoparticles (785 nm, cit.[36]). In the current work, the Fe-Ni/H-Beta-300 spent

602   catalyst from the batch experiment of isoeugenol hydrodeoxygenation (ca. 8 wt% of coke, Table

603   4) was analysed in both powder and thin pressed pellet form. However, all measurements

604   performed at different conditions resulted in one big peak (Figure S14) attributed to the strong

605   fluorescence interference.[33,37]

3.2   Activity and selectivity of the FeNi/H-Beta-300 catalyst in hydrodeoxygenation

607   A set of solventless experiments over the reference 5-5 wt% Fe-Ni/H-Beta-300 catalyst

608   (sieved fraction 150-180 μm) has been performed in batch and continuous modes. Isoeugenol

609   and its hydrogenated intermediate dihydroeugenol were used as feedstock. It should be also

610   pointed out that in the case of isoeugenol as a reactant, the reaction proceeds via rapid

611   hydrogenation to dihydroeugenol, even in the absence of any catalyst, which is in line with the

612   literature.[11] Therefore, catalytic results of IE HDO also comprise the conversion of the

613   consecutive step, i.e. conversion of dihydroeugenol.

3.2.1 Batch experiments

615   Solventless experiments with and without injection of the reactant into the preheated reactor

616   with a catalyst were carried out at 200 °C (1 h) - 250 °C (1 h) - 300°C (1 h), 30 bar with the

617   reactant-to-catalyst weight ratio of 25 in the batch mode. The results from the batch experiments

618   are summarized in Table 5 and displayed in Figure S15. Low-cost FeNi/H-Beta-300 catalyst

619   tested in isoeugenol hydrodeoxygenation (IE HDO) in a batch reactor exhibited low

620   dihydroeugenol conversion (Figure S15a) with low selectivity to the desired oxygen-free

621   compounds (Figure S15b) accompanied by a rapid catalyst deactivation compared to the IE

622   HDO with the solvent over FeNi/H-Y-5.1 catalysts.[11] This could be attributed to strong

623   adsorption of highly viscous isoeugenol on the surface of the catalyst (Figure S15c, d) which is

624   also in line with a lower liquid phase mass balance closure compared to the experiments with

625   the first intermediate, dihydroeugenol, as a raw material (Table 5). The main product of IE

626   HDO was dihydroeugenol with the yield of 77%, while the yield of oxygen-free products was

627   only 3%. For comparison, IE HDO batch experiment without a catalyst[11] performed under

628   similar conditions, i.e. 200 °C and 20 bar, showed 17% conversion of isoeugenol to

629   dihydroeugenol without any other products. After 4 h, in co-processing of n-hexadecane with

630   lignin derived isoeugenol over 5-5 wt% FeNi/H-Y-5.1 catalyst performed in the batch at 300

631   °C and 30 bar, the complete conversion of both isoeugenol and dihydroeugenol was obtained

632   with only desired oxygen-free compounds.[11] As a comparison with IE HDO in the presence of

633   a solvent, typically a high conversion of DHE has also been obtained with Ni catalyst. For

634   example, the batch experiment of IE HDO, carried out at 250 °C, 30 bar with 10 wt% Ni/ZrO_2

635   catalyst (63 μm) with 0.05 g isoeugenol in 50 mL of dodecane, displayed complete conversion

636   of isoeugenol and 95% conversion of dihydroeugenol, however, the yield of OFC (oxygen-free

637   compounds) was only 16% with an extremely low liquid phase mass balance closure below

638   20%.[38] A 75% yield of OFC was obtained over a non acidic Ni-SBA-15 in IE HDO at 300 °C,

639   30 bar H_2 using dodecane as a solvent.[39] In the same work,[39] Ni-SZ-SBA-15 containing

640   sulphated ZrO_2 gave only very low HDO activity, which was explained by location of the acid

641   sites both inside and outside SBA-15, whereas nickel particles were partially located inside the

642   SBA-15 structure. In the case of IE HDO in dodecane in the batch reactor over 11 wt% Ni/SiO_2

643   and 20 wt% Ni/graphite, the yield of OFC was 60% and 44%, respectively, at complete

644   conversion of both isoeugenol and dihydroeugenol after 4 h at 300 °C, 30 bar H_2 with the liquid

645   phase mass balance closure ca. 70%.[40] Futhermore with the noble metal catalyst, the batch

646   experiment of IE HDO, carried out at 300 °C, 30 bar H_2 with 0.1 g 5 wt% Pt catalyst over

647   activated carbon (63 μm) with 0.05 g isoeugenol in 50 mL of dodecane, also displayed complete

648   conversion of both isoeugenol and dihydroeugenol. However, the yield of OFC was only 31%.[41]

649   A similar experiment over the bimetallic 4-4 wt% Pt-Re/Sibunit catalyst (63 μm) carried out

650   under the same conditions demonstrated full conversion with 84% yield of OFC.[41]

651   In the case of dihydroeugenol (DHE) as a starting material, the initial reaction rate of

652   dihydroeugenol HDO was ca 3-fold lower for the experiment without the injection of the

653   reactant on the preheated catalyst, which could be attributed to the strong adsorption of the

654   reactant on the catalyst during the heating period of the reactor. When comparing the product

655   distribution between DHE and IE HDO in a batch reactor in the current study, ca. two-fold yield

656   of the desired oxygen-free compounds (6%) and a slightly higher water content (0.9%) were

657   gained at the same DHE conversion level (19%) as for IE HDO performed under the same

658   conditions. Except soluble coke species composition (Figure S12) and the initial reaction rate

659   and turnover frequency (Table 5), the results of DHE HDO from both experiments, i.e. with

660   and without an injection on the preheated catalyst, were comparable (Table 5). No heavy

661   compounds were detected by GC-FID, short column analysis, or SEC analysis of the liquid

662   phase. In the gas phase, only hydrogen was detected in all cases of the batch experiments.

663   For comparison with the literature,[42] DHE conversion of 34% was observed in the batch

664   reactor over a dual catalyst system, 0.1 g Ru/C and 0.2 g Nb_2O_5, at 250 °C and 6 bar of hydrogen

665   in the mixture of DHE (0.2 mL), MeOH (0.8 mL) and distilled water (12 mL) giving 4% yield

666   of the desired oxygen-free compounds and S_{OCC}/S_{OFC} equal to 90/10 in DHE HDO performed.

667   It should also be noted, that after 4 h DHE was fully converted giving the S_{OCC}/S_{OFC} ratio equal

668   to 69/31.[42] It can be concluded that more efficient deoxygenation of DHE was obtained in the

669   presence of the solvent, as expected.

670   *Table 5. Catalytic results (in %) from the batch experiments performed at 250-300 °C, 30 bar with 2.2 g of catalyst,*
671   *after 3 h. Legend: r^0 – initial reaction rate of the reactant (1 minute, 250 °C) in mol/g/h, TOF^0 – initial turnover*
672   *frequency in 1/h, X_{IE} – isoeugenol conversion, X_{DHE} – dihydroeugenol conversion, $CB_{(l)}$ – the liquid phase carbon*
673   *balance closure, S – selectivity, Y – yield, OCC – oxygen-containing compounds, OFC – oxygen-free compounds.*

Entry	Reactant	Notes	r^0	TOF^0	X_{IE}	X_{DHE}	$CB_{(l)}$	S_{OCC}/S_{OFC}	Y_{OCC}	Y_{OFC}	Y_{H2O}
1	isoeugenol	no injection	-	-	100	19	83	96*/4	80**	3	0.6

| 2 | dihydroeugenol | no injection | 0.12 | 77 | - | 19 | 97 | 64/36 | 11 | 6 | 0.9 |
| 3 | | injection | 0.37 | 231 | - | 20 | 95 | 72/28 | 12 | 5 | 0.8 |

674   * 77% was dihydroeugenol, ** 64% was dihydroeugenol

675   *3.2.2 Continuous experiments*

676   Experiments in the continuous mode were performed at 250-300 °C, 30 bar with 0.1-0.3 g

677   of the catalyst with 0.04 mL/min of the reactant liquid flow, WHSV of 8-25 $g_{reactant}/g_{catalyst}/h$,

678   and a 15-fold excess of hydrogen. The results from the continuous experiments are summarized

679   in Table 6 and displayed in Figure S16 (IE HDO), and Figure S18 (DHE HDO).

680

681 *Table 6. Catalytic results (in %) from the continuous experiments performed at 250-300 °C, 30 bar with 0.1-0.3 g of catalyst. Legend: r^0 – initial reaction rate of dihydroeugenol*
682 *HDO (1 min, 300 °C) in mol/g/h, TOF^0 – initial turnover frequency of dihydroeugenol HDO in 1/h, X_{IE} – isoeugenol conversion, X_{DHE} – dihydroeugenol conversion, CB –*
683 *carbon balance closure, MB – mass balance closure, (l) – the liquid phase, (g) – the gas phase, (ad) – heavy compounds adsorbed on the catalyst (coke), S – selectivity, Y –*
684 *yield, OCC – oxygen-containing compounds, OFC – oxygen-free compounds, Δ - initial deactivation in 30 min of time-on-stream (TOS) (in % per min).*

| Entry	DHE/IE	Conditions	in 1 min of time-on-stream							in 5 h of time-on-stream								
			r^0_{DHE}	TOF^0_{DHE}	X^0_{IE}	X^0_{DHE}	$S^0_{OCC(DHE)}/S^0_{OFC}$	Y^0_{OCC}	Y^0_{OFC}	X_{IE}	X_{DHE}	$CB_{(l)}$	$S_{OCC(DHE)}/S_{OFC}$	Y_{OCC}	Y_{OFC}	Y_{H2O}	ΔX_{DHE}	ΔS_{OFC}
4	IE	300 °C, 0.2g	0.11	70	96	72	61(41)/39	39.5	25.3	100	43	63	98(90)/2	62.2	1.5	1.5	0.53	0.64
5	IE	300 °C, 0.3g	0.08	49	100	99	24(1)/76	18.2	58.2	100	30	78	96(89)/4	75.3	3.2	1.3	1.09	1.20
6	IE	275 °C, 0.3g	0.07	46	100	91	19(11)/81	16.1	68.3	100	23	83	94(92)/6	79.2	4.7	0.8	1.01	1.33
7	IE	250 °C, 0.3g	0.07	43	100	90	14(11)/86	12.0	71.1	100	15	90	94(93)/6	85.5	5.6	1.3	1.24	1.47
8a	DHE**	300 °C, 0.1g	0.06	36	-	47	38/62	9.3	15.1	-	9	95	45/55	2.2	2.7	0.7	0.69	0.07
8b			0.02	12	-	15	66/34	5.3	2.7	-	7*	98*	77/23*	1.3*	4.4*	0.2	0.00	0.03
9a	DHE**	300 °C, 0.3g	0.06	35	-	78	20/80	12.4	50.2	-	23	93	62/38	11.3	6.9	1.8	0.72	0.78
9b			0.03	20	-	45	71/29	11.9	4.7	-	17	96	65/35	8.7	4.7	0.7	0.33	-

685   * 3h TOS, ** two runs

686   Hydrodeoxygenation of isoeugenol (IE HDO) in the continuous mode revealed rapid catalyst

687   deactivation during the first hour of time-on-stream (ΔX_{DHE} 1-1.2% per minute over 0.3 g of

688   catalyst, Figure 10a). A slightly slower deactivation was observed in hydrodeoxygenation of

689   dihydroeugenol (DHE HDO), a first intermediate of isoeugenol HDO (ΔX_{DHE} 0.7% per minute

690   over 0.3 g of catalyst, Figure 10b). In both cases, the yield of the desired oxygen-free

691   compounds (OFC, Figure 10c,d) decreased during the first hour of time-on-stream too. The

692   product distribution of the individual oxygen-free and oxygen-containing compounds detected

693   in the liquid phase is presented in Figures S19 and S20.

694   In the gas phase (Figure S21), mainly methane, one unknown product, and methanol were

695   detected. While methane and methanol decreased with increasing catalyst deactivation and

696   water formation, the concentration of the unknown product had the opposite trend. Ethane,

697   propane, butane, isobutene, and carbon oxides were detected in negligible amounts. Overall,

698   the total concentration of the gas-phase products decreased with decreasing DHE conversion in

699   all the cases of continuous experiments.

a)

b)
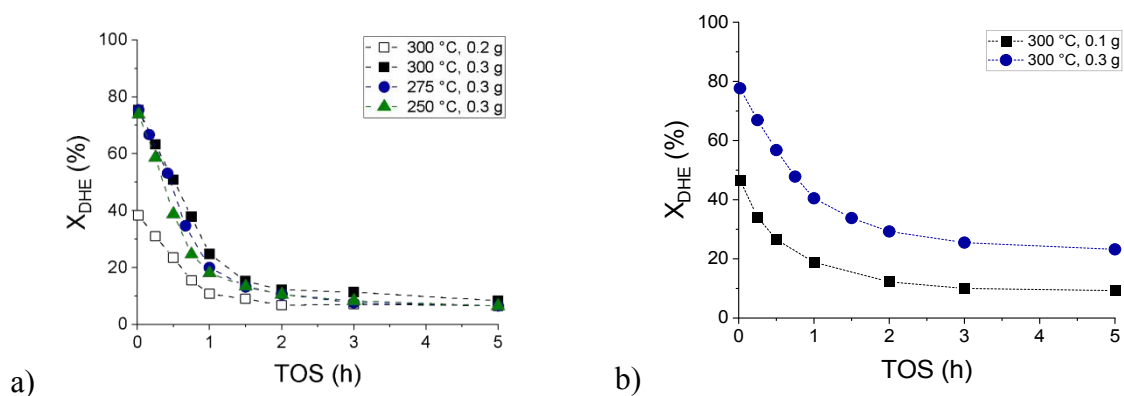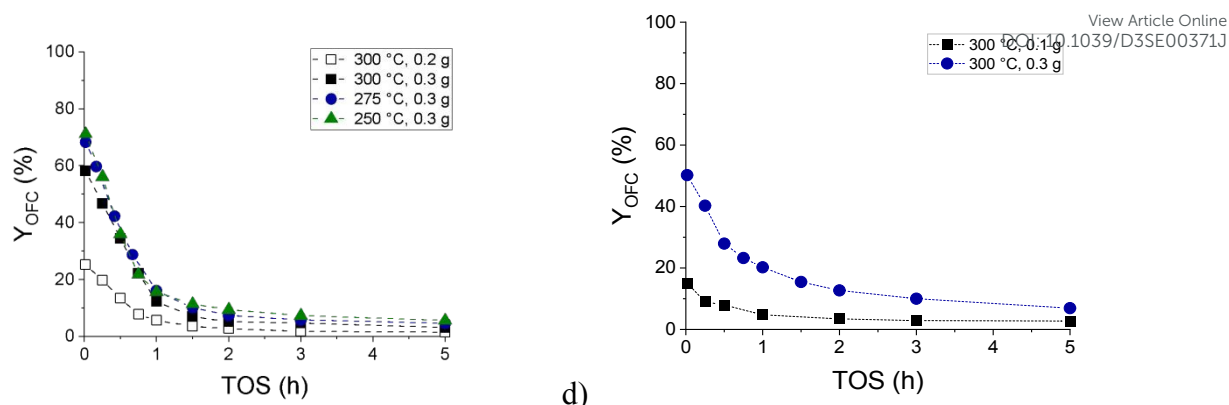
700 *Figure 10. Dihydroeugenol conversion as a function of time-on-stream in a) isoeugenol hydrodeoxygenation, b)*
701 *dihydroeugenol hydrodeoxygenation; yield of the oxygen-free compounds as a function of time-on-stream in a)*
702 *isoeugenol hydrodeoxygenation, b) dihydroeugenol hydrodeoxygenation. Conditions: 250-300 °C, 30 bar, 0.1-0.3*
703 *g of catalyst with 0.04 mL/min of liquid flow and a 15-fold excess of hydrogen.*
704

705   IE HDO performed at different temperatures demonstrated a higher initial selectivity to OFC

706   at a lower temperature. The apparent activation energy of dihydroeugenol hydrodeoxygenation

707   over FeNi/H-Beta-300 catalyst (150-180 μm) in solventless isoeugenol HDO was calculated to

708   be 6.3 kJ/mol (Figure S22). This value is 2.4-fold lower than it was reported in,[41] i.e. 15 kJ/mol,

709   for 0.3 g granulated PtRe(1:1)/Sibunit catalyst (1 mm) at 75-200 °C, 30 bar of H_2 and 0.5

710   mL/min liquid flow of 0.012 M isoeugenol in dodecane. The activation energy in the kinetic

711   study of dihydroeugenol hydrodeoxygenation, without hydrogenation step of isoeugenol, in the

712   packed-bed microreactor over sulfided $NiO/MoO_3/Al_2O_3$ catalyst (75-150 μm) at 200-450 °C

713   and 20.7 bar was calculated to be 34 kJ/mol.[43] Note that the lower activation energy of DHE

714   obtained in the current work from IE HDO in practice can depend not only on the catalyst type

715   but also on the catalyst deactivation, commonly modeled as an exponential decay function of

716   active sites with TOS,[44] appearing in the first step of isoeugenol hydrogenation. A low value of

717   apparent activation energy in the current work could also be attributed to the presence of mass

718   transport limitation regime in non-diluted reaction system with significantly lower ratio of

719   reactant-to-catalyst.

720   The mass transport limitations were estimated for DHE HDO in the continuous mode (Table

721   6, entry 8a) assuming the spherical catalyst particles and the first-order reaction.[45-47] The Mears

722   criterion of external mass transfer limitation ($C_{Mears} < 0.15$) for H_2 dissolved in DHE and for

723   DHE was calculated to be 4423 and $2.3 \cdot 10^{-4}$, respectively. Low values of the Damköhler

724   number (Da = $7.8 \cdot 10^{-4}$) and the Thiele modulus ($\phi = 2.8 \cdot 10^{-5}$) giving subsequently the catalyst

725   effectiveness factor equal to one also pointed out on absence of external or internal mass transfer

726   limitations of the liquid compounds. It can be concluded that the low apparent activation energy

727   obtained in the current work for DHE HDO was affected by both external mass transfer

728   limitation of hydrogen dissolved in dihydroeugenol and by the rapid catalyst deactivation in the

729   initial isoeugenol hydrogenation.

730   To elucidate the catalyst deactivation, the catalyst was consecutively reused in

731   dihydroeugenol hydrodeoxygenation after in-situ regeneration, which was performed by simply

732   flushing the catalyst with hydrogen flow of 40 mL/min overnight at the reaction temperature

733   (Table 6, entry 8) or by coke oxidation increasing temperature step-by-step from 200 °C to 400

734   °C, with the heating ramp of 2 °C/min with 40 mL/min of 5 vol% oxygen in argon after flushing

735   with argon (Table 6, entry 9). In the latter case, the outlet gas stream was monitored by

736   microGC-TCD (Figure S17) and after regeneration, the catalyst was flushed with argon again

737   and reduced by the same procedure as described above.

738   In the first case, when the spent catalyst was flushed out in the hydrogen flow, the initial

739   conversion of dihydroeugenol in the second run was only ca. 30 % of the first run. After 3 h

740   with time-on-stream, the conversion level was just by ca. 20% lower than with the fresh catalyst,

741   while selectivity to the desired oxygen-free compounds was lower by ca. 60% and Y_{OCC}/Y_{OFC}

742   ratio by ca 70% (Figure S18). On the other hand, in the second case, when the coke in the spent

743   catalyst was oxidized in 5 vol% of oxygen in argon flow at up to 400 °C, the initial conversion

744 of dihydroeugenol during the second run was two-fold higher than in case of flushing in

745 hydrogen, i.e. ca. 60 % of the initial value compared to the first run. The initial reaction rate

746 dropped only by 1.7-fold for the second run. After 5 h of time-on-stream, the conversion level

747 was lowered by ca. 25% compared to the fresh catalyst, while selectivity to the desired oxygen-

748 free compounds was lower only by ca 8% and Y_{OCC}/Y_{OFC} ratio by ca 10% (Figure S18). Overall,

749 it can be concluded that in-situ regeneration at up to 400 °C in the presence of oxygen was

750 successful resulting in slightly lower activity and similar selectivity of the consecutively reused

751 catalyst compared to the results obtained from the fresh one. A slightly lower reaction rate of

752 DHE, 0.4 mol/g/h, was obtained from HDO of DHE over sulfided $NiO/MoO_3/Al_2O_3$ catalyst at

753 300 °C and 14.3 bar with 2.1 mol/L DHE concentration in hexane.[43]

754 As mentioned above, catalyst deactivation was directly related to the formation of aliphatic

755 coke on the spent catalyst, which led to a decrease in its specific surface area (Figure 9).

756 Furthermore, it was observed that the rate of coke formation (Rc, μg of coke/mg of catalyst/h)

757 increased with increasing dihydroeugenol conversion (Figure 11a) and with increasing yield of

758 water (Figure 11b) as a side product. This applies to all experiments independently of the

759 reaction system, temperature, or reactant. Simultaneously, the liquid phase carbon balance

760 closure decreased with the increasing amount of coke in line with the strong adsorption of heavy

761 compounds on the catalyst. Analogously, the coke formation was also the considered as the

762 reason for catalyst deactivation in bio-oil hydrodeoxygenation on Ni/H-ZSM-5 and Ni-Cu/H-

763 ZSM-5 catalysts.[48] The rate of coke formation of 10 μg of coke/mg of catalyst/h reported over

764 Ni/HZSM-5 catalyst in bio-oil hydrodeoxygenation at 300 °C[47] was comparable with the lowest

765 rate of coke formation of 12 μg of coke/mg of catalyst/h obtained in the current work at the

766 lowest DHE conversion. A similar range of the rate of coke formation as in the current work

767 (12-37 μg of coke/mg of catalyst/h) was also obtained over 10 wt% Fe/SiO_2 catalyst in guaiacol

768   HDO at 400 °C in the presence of H_2, CH_4 or H_2O (13-36 μg of coke/mg of catalyst/h). A

769   lower rate of coke formation 8 μg of coke/mg of catalyst/h was observed in HDO of the bio-oil

770   in a continuous-flow two-stage catalytic reactor system that contained a mild hydrogenation

771   zone at 130 °C over Ru/C as the catalyst followed by a more severe HDO zone between 300–

772   400 °C over a Pt/ZrP catalyst.[50]

773

a)

b)

d)

c)
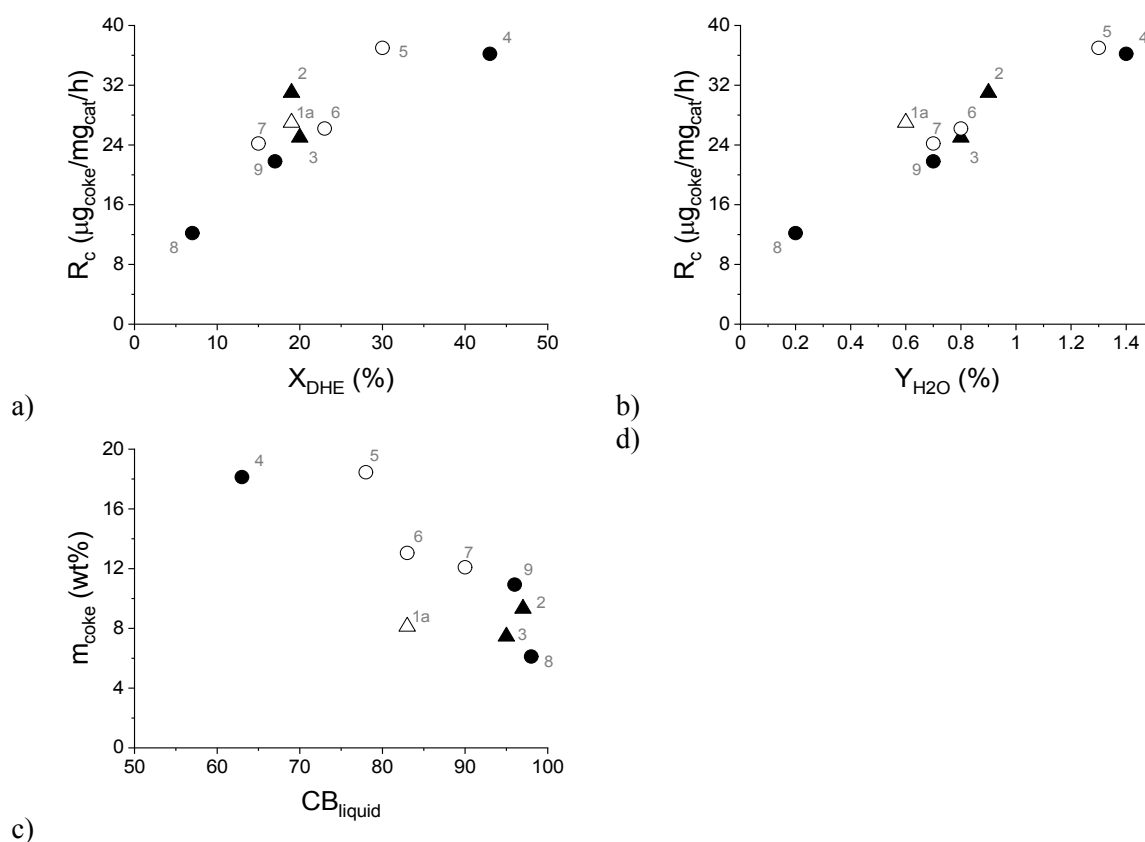
774   *Figure 11. Formation rate of coke as a function of: a) dihydroeugenol conversion, b) yield of water; c) amount of*
775   *coke as a function of the liquid phase carbon balance closure. Conditions: solventless hydrodeoxygenation over*
776   *0.1-0.3 g of FeNi/H-Beta-300 (150-180 μm) catalyst at 250-300 °C, 30 bar of H_2, 0.04 mL/min of liquid flow and*
777   *a 15-fold excess of hydrogen. Legend: spent catalyst from the batch experiment (triangle), the spent catalyst from*
778   *the continuous experiments (circle), spent catalyst from IE HDO (open symbols) and the spent catalyst from DHE*
779   *HDO (black symbols). Notation is the same as in the Table 4.*

780

781 ## 4 Conclusions

782   A low-cost bimetallic bifunctional 5-5 wt% FeNi/H-Beta-300 catalyst synthesized by the

783   subsequent incipient wetness impregnation was investigated in hydrodeoxygenation in the

784   batch and continuous modes. Solventless experiments were performed with lignin-derived

785   model compounds isoeugenol or dihydroeugenol. The liquid phase of the reaction mixture was

786   analysed by GC-FID, GC-MS and Karl-Fischer titration while the gas phase by microGC-TCD.

787   Characterization of the fresh and spent catalysts was made by several physico-chemical

788   methods. The spent catalyst was regenerated in-situ and consecutively reused.

789   After metals impregnation, the total acidity of the catalyst remained mild, 104 μmol/g, while

790   the ratio of the Brønsted and Lewis acid sites significantly decreased from 6 to 0.8. The

791   nanoparticle size of Fe and Ni metals of 6 and 20 nm, respectively, was determined by fitting

792   of Kernel Smooth distribution from TEM. The results from Mössbauer spectroscopy, XAS,

793   SEM-EDX, and TPR confirmed metal-metal and metal-support interactions. After the

794   reduction, 93% of iron was in the metallic form. In the FeNi alloy distribution of both metals

795   was random. The specific surface area for the fresh catalyst was 516 m^2/g comprising 81 vol%

796   micropores. After the reaction, a significant drop in both the specific surface area and pore

797   volume of the catalyst was observed due to formation of filamentous type coke. The specific

798   surface area of the spent catalysts, tested under different conditions, linearly decreased with the

799   increasing amounts of coke determined by TGA analysis (6-19 wt%). The extracted soluble

800   coke species were predominantly identified as the aliphatic ones. After in-situ regeneration by

801   coke oxidation, the mesoporosity was fully regenerated while 80% of the specific surface area

802   and microporosity was restored in the regenerated catalyst compared to the fresh one.

803   The batch experiments resulted in low activity and poor selectivity to the desired oxygen-

804   free compounds accompanied by a rapid catalyst deactivation. The experiments in the

805 continuous mode demonstrated slower catalyst deactivation showing not only a decrease of

806 conversion but also significant selectivity changes with increasing time-on-stream. A slightly

807 slower catalyst deactivation was observed in hydrodeoxygenation of dihydroeugenol (ΔX_{DHE}

808 0.7% per minute) compared to isoeugenol hydrodeoxygenation in the continuous mode. The

809 apparent activation energy of dihydroeugenol hydrodeoxygenation over FeNi/H-Beta-300

810 catalyst (150-180 μm) in solventless isoeugenol hydrodeoxygenation was calculated to be 6.3

811 kJ/mol, which can be ascribed to external mass transfer limitations and the catalyst deactivation

812 in isoeugenol hydrogenation. Conversion of 78% of the initial dihydroeugenol with 80% of

813 selectivity to the desired oxygen-free compounds was obtained over 0.3 g of catalyst at 300 °C

814 and 30 bar of hydrogen with a residence time 12 min. Oxidative regeneration at up to 400 °C

815 was successfully done resulting in a slightly lower catalyst activity and similar selectivity of

816 the regenerated catalyst compared to the fresh one.

817 ## 5 Supporting Information

818 Definitions, catalyst characterization results: SEM, BSE, EDX, ICP-OES, TEM, EXAS, O_2-

819 TPO, GC-MS analysis of the extracted soluble coke species, Raman, catalytic results.

820 ## 6 Acknowledgments

Sustainable Energy & Fuels Accepted Manuscript

7 References

1. A. A. Dwiatmoko, J. Seo, J. W. Choi, D. J. Suh, J. M. Jae, and J. M. Ha, Improved activity of a CaCO₃-supported Ru catalyst for the hydrodeoxygenation of eugenol as a model lignin-derived phenolic compound, *Catal. Commun.,* **2019**, *127*, 45-50, DOI: 10.1016/j.catcom.2019.04.024.

2. M. X. Zhao, J. Hu, P. Lu, S. L. Wu, C. Liu, and Y. H. Sun, Efficient hydrodeoxygenation of lignin-derived bio-oil to hydrocarbon fuels over bifunctional RuCoWx/NC catalysts, *Fuel,* **2022**, *326*, DOI: 10.1016/j.fuel.2022.125020.

3. A. Bjelic, M. Grilc, and B. Likozar, Bifunctional metallic-acidic mechanisms of hydrodeoxygenation of eugenol as lignin model compound over supported Cu, Ni, Pd, Pt, Rh and Ru catalyst materials, *Chem. Eng. J.,* **2020**, *394*, 14, DOI: 10.1016/j.cej.2020.124914.

4. X. K. Yue, S. Zhang, N. Z. Shang, S. T. Gao, Z. Wang, and C. Wang, Porous organic polymer supported PdAg bimetallic catalyst for the hydrodeoxygenation of lignin-derived species, *Renew. Ener.,* **2020**, *149*, 600-608, DOI: 10.1016/j.renene.2019.12.066.

5. M. X. Zhao, J. Hu, S. L. Wu, L. Yang, X. An, P. Yuan, and P. Lu, Hydrodeoxygenation of lignin-derived phenolics over facile prepared bimetallic RuCoNx/NC, *Fuel,* **2022**, *308,* DOI: 10.1016/j.fuel.2021.121979.

6. T. Liu, Z. Tian, W. Zhang, B. Luo, L. Lei, C. Wang, J. Liu, R. Shu, and Y. Chen, Selective hydrodeoxygenation of lignin-derived phenols to alkyl cyclohexanols over highly dispersed RuFe bimetallic catalysts, *Fuel,* **2023**, *339*, 12916, DOI: 10.1016/j.fuel.2022.126916.

7. S. Khan, K. M. Qureshi, A. N. K. Lup, M. F. A. Patah, and W. Daud, Role of Ni-Fe/ZSM-5/SAPO-11 bifunctional catalyst on hydrodeoxygenation of palm oil and triolein for alternative jet fuel production, *Biomass Bioenerg.,* **2022**, *164,* 106563, DOI: 10.1016/j.biombioe.2022.106563.

8. J. W. Zhou, and W. An, Unravelling the role of oxophilic metal in promoting the deoxygenation of catechol on Ni-based alloy catalysts, *Catal. Sci. Technol.,* **2020**, *10,* 6849-6859, DOI: 10.1039/d0cy01361g.

9. L. Bomont, M. Alda-Onggar, V. Fedorov, A. Aho, J. Peltonen, K. Eranen, M. Peurla, N. Kumar, J. Warna, V. Russo, P. Mäki-Arvela, H. Grénman, M. Lindblad, and D. Yu. Murzin, Production of cycloalkanes in hydrodeoxygenation of isoeugenol over Pt- and Ir-modified bifunctional catalysts, *Eur. J. Inorg. Chem.,* **2018**, *24,* 2841-2854, DOI: 10.1002/ejic.201800391.

10. N. K. G. Silva, R. A. R. Ferreira, R. M. Ribas, R. S. Monteiro, M. A. S. Barrozo, and R. R. Soares, Gas-phase hydrodeoxygenation (HDO) of guaiacol over Pt/Al₂O₃ catalyst promoted by Nb₂O₅, *Fuel,* **2021**, *287,* 119509, DOI: 10.1016/j.fuel.2020.119509.

11. Z. Vajglová, B. Gauli, P. Mäki-Arvela, I. L. Simakova, N. Kumar, K. Eränen, T. Tirri, R. Lassfolk, M. Peurla, D. E. Doronkin, and D. Yu. Murzin, Co-Processing of fossil feedstock with lignin-derived model compound isoeugenol over Fe-Ni/H-Y-5.1 catalysts, *J. Catal.,* **2023**, *421,* 101-116, DOI: 10.1016/j.jcat.2023.03.016.

12. Z. Vajglová, B. Gauli, P. Mäki-Arvela, N. Kumar, K. Eränen, J. Warna, R. Lassfolk, I. L. Simakova, I. Provirin, M. Peurla, J. Lindén, H. Huhtinen, P. Petriina, D. E. Doronkin, and D. Yu. Murzin, Interactions between iron and nickel in Fe-Ni nanoparticles on Y zeolite for co-

873 processing of fossil feedstock with lignin-derived isoeugenol, *ACS Appl. Nano Mater.,* **2023**,
874 in print, DOI: 10.1021/acsanm.3c00620

875 13.   ImageJ program, https://imagej.net/Welcome (accessed March 2023).

876 14.   B. Ravel, and M. Newville, Athena, Artemis, Hephaestus: data analysis for X-ray
877 absorption spectroscopy using IFEFFIT, *J. Synchrotron Radiat.,* **2005**, *12*, 537-541, DOI:
878 10.1107/s0909049505012719.

879 15.   M. I. Urseanu, J. G. Boelhouwer, H. J. M. Bosman, J. C. Schroijen, and G. Kwant,
880 Estimation of trickle-to-pulse flow regime transition and pressure drop in high-pressure trickle
881 bed   reactors   with   organic   liquids,   *Chem.   Eng.   J.,*   **2005**,   *111*,   5-11,   DOI:
882 10.1016/j.cej.2005.04.015.

883 16.   G. Mary, A. Esmaeili, and J. Chaouki, Simulation of the selective hydrogenation of C-3-
884 cut in the liquid phase, *Int. J. Chem. React. Eng.,* **2016**, *14*, 859-874, DOI: 10.1515/ijcre-2015-
885 0095.

886 17.   Z. Vajglová, N. Kumar, M. Peurla, J. Peltonen, I. Heinmaa, and D. Yu. Murzin, Synthesis
887 and physicochemical characterization of beta zeolite-bentonite composite materials for shaped
888 catalysts, *Catal. Sci. Technol.,* **2018**, *8*, 6150-6162, DOI: 10.1039/c8cy01951g.

889 18.   X. Y. Yang, X. W. Cheng, A. A. Elzatahry, J. Y. Chen, A. Alghamdi, and Y. H. Deng,
890 Recyclable Fenton-like catalyst based on zeolite Y supported ultrafine, highly-dispersed Fe_2O_3
891 nanoparticles for removal of organics under mild conditions, *Chin. Chem. Lett.,* **2019**, *30*, 324-
892 330, DOI: 10.1016/j.cclet.2018.06.026.

893 19.   J. J. F. Scholten, A. P. Pijpers, and A. M. L. Hustings, Surface characterization of
894 supported and nonsupported hydrogenation catalysts, *Catal. Rev. Sci. Eng.,* **1985**, *27*, 151-206,
895 DOI: 10.1080/01614948509342359.

896 20.   A. J. Plomp, H. Vuori, A. O. I. Krause, K. P. de Jong, and J. H. Bitter, Particle size effects
897 for   carbon   nanofiber   supported   platinum   and   ruthenium   catalysts   for   the   selective
898 hydrogenation   of   cinnamaldehyde.   *Appl.   Catal.   A-Gen.,*   **2008**,   *351*,   9-15,   DOI:
899 10.1016/j.apcata.2008.08.018.

900 21.   G. Bergeret, and P. Gallezot, Particle size and dispersion measurements, *Handbook of
901 Heterogenous Catalysis*, Ertl, G., Knözinger, H., Schüth, F., Weitkamp, J. Eds.; Wiley-VCH
902 Verlag GmbH & Co. KGaA, 2008.

903 22.   D. Kubička, N. Kumar, T. Venalainen, H. Karhu, I Kubičkova, H. Osterholm, and D. Yu.
904 Murzin, Metal-support interactions in zeolite-supported noble metals: influence of metal
905 crystallites   on   the   support   acidity,   *J.   Phys.   Chem.   B,*   **2006**,   *110*,   4937-4946,   DOI:
906 10.1021/jp055754k.

907 23.   H. Metiu, S. Chretien, Z. P. Hu, B. Li, and X. Y. Sun, Chemistry of Lewis acid-base pairs
908 on oxide surfaces, *J. Phys. Chem. C,* **2012**, *116*, 10439-10450, DOI: 10.1021/jp301341t.

909 24.   A. Puig-Molina, F. M. Cano, and T. V. W. Janssens, The Cu promoter in an iron-
910 chromium-oxide based water-gas shift catalyst under industrial conditions studied by in-situ
911 XAFS, *J. Phys. Chem. C,* **2010**, *114*, 15410-15416, DOI: 10.1021/jp1035103.

912 25.   M. Nagai, O. Uchino, J. Okubo, and S. Omi, TPR and XPS studies of iron-exchanged Y
913 zeolites and their activity during dibenzothiophene hydrodesulfurization. *Stud. Surf. Sci. Catal.,*
914 **1997**, *105*, 989-995. DOI: 10.1016/S0167-2991(97)80731-8.

915 26. N. Czuma, K. Zarebska, M. Motak, M. E. Galvez, and P. Da Costa, Ni/zeolite X derived
916 from fly ash as catalysts for CO_2 methanation, *Fuel,* **2020**, *267,* 117139, DOI:
917 10.1016/j.fuel.2020.117139.

918 27. S. E. Eliana-Misi, A. Ramli, and F. H. Rahman, Characterization of the structure feature
919 of bimetallic Fe-Ni catalysts, *J. Appl. Sci.,* **2011**, *11*, 1297-1302, DOI:
920 10.3923/jas.2011.1297.1302.

921 28. Z. X. Cheng, X. G. Zhao, J. L. Li, and Q. M. Zhu, Role of support in CO_2 reforming of
922 CH_4 over a Ni/gamma-Al_2O_3 catalyst, *Appl. Catal. A-Gen.,* **2001**, *205,* 31-36, DOI:
923 10.1016/s0926-860x(00)00560-3.

924 29. O. A. Sahraei, A. Desgagnes, F. Larachi, and M. C. Iliuta, Ni-Fe catalyst derived from
925 mixed oxides Fe/Mg-bearing metallurgical waste for hydrogen production by steam reforming
926 of biodiesel by-product: investigation of catalyst synthesis parameters and temperature
927 dependency of the reaction network, *Appl. Catal. B-Environ.,* **2020**, *279*, 119330, DOI:
928 10.1016/j.apcatb.2020.119330.

929 30. M.C. Sánchez-Sánchez, R.M. Navarro, J.L.G. Frierro, Ethanol stam reforming over
930 Ni/La-Al2O3 catalysts: influence of lanthanum loading, Catal. Today, 2007, 129, 336-345,
931 DOI: 10.1016/j.cattod.2006.10.013

932 31. J. Cain, A. Laskin, M. R. Kholghy, M. J. Thomson, and H. Wang, Molecular
933 characterization of organic content of soot along the centerline of a coflow diffusion flame,
934 *Phys. Chem. Chem. Phys.,* **2014**, *16*, 25862-25875, DOI: 10.1039/c4cp03330b.

935 32. C. Li, and P. C. Stair, Coke formation in zeolites studied by a new technique: ultraviolet
936 resonance Raman spectroscopy, *Stud. Surf. Sci. Catal.*, **1997**, *105*, 599-606, DOI:
937 10.1016/S0167-2991(97)80606-4.

938 33. H. Z. Wang, L. L. Sun, Z. J. Sui, Y. A. Zhu, G. H. Ye, D. Chen, X. G. Zhou, and W. K.
939 Yuan, Coke formation on Pt-Sn/Al_2O_3 catalyst for propane dehydrogenation, *Ind. Eng. Chem.*
940 *Res.,* **2018**, *57*, 8647-8654, DOI: 10.1021/acs.iecr.8b01313.

941 34. C. C. Zhang, S. Hartlaub, I. Petrovic, and B. Yilmaz, Raman Spectroscopy
942 characterization of amorphous coke generated in industrial processes, *ACS Omega,* **2022**, *7*,
943 2565-2570, DOI: 10.1021/acsomega.1c03456.

944 35. S. R. Bare, F. D. Vila, M. E. Charochak, S. Prabhakar, W. J. Bradley, C. Jaye, D. A.
945 Fischer, S. T. Hayashi, S. A. Bradley, and J. J. Rehr, Characterization of coke on a Pt-
946 Re/gamma-Al_2O_3 Re-forming catalyst: experimental and theoretical study, *ACS Catal.,* **2017**,
947 *7*, 1452-1461, DOI: 10.1021/acscatal.6b02785.

948 36. P. J. Wang, D. Zhang, L. S. Zhang, and Y. Fang, The SERS study of graphene deposited
949 by gold nanoparticles with 785 nm excitation, *Chem. Phys. Lett.,* **2013**, *556,* 146-150, DOI:
950 10.1016/j.cplett.2012.11.018.

951 37. P. D. Green, C. A. Johnson, and K. M. Thomas, Applications of laser Raman microprobe
952 spectroscopy to the characterization of coals and cokes, *Fuel,* **1983**, *62*, 1013-1023, DOI:
953 10.1016/0016-2361(83)90134-5.

954 38. M. Alda-Onggar, P. Mäki-Arvela, A. Aho, I. L. Simakova, and D. Yu. Murzin,
955 Hydrodeoxygenation of phenolic model compounds over zirconia supported Ir and Ni-catalysts,
956 *React. Kinet. Mech. Catal.,* **2019**, *126*, 737-759, DOI: 10.1007/s11144-018-1502-1.

View Article Online
DOI: 10.1039/D3SE00371J

957   39.   S. Tieuli, P. Mäki-Arvela, M. Peurla, K. Eränen, J Warna, G. Cruciani, F. Menegazzo, D.
958   Yu. Murzin, and M. Signoretto, Hydrodeoxygenation of isoeugenol over Ni-SBA-15: Kinetics
959   and modelling, *Appl. Catal. A-Gen.,* **2019**, *580,* 1-10, DOI: 10.1016/j.apcata.2019.04.028.

960   40.   C. Lindfors, P. Mäki-Arvela, P. Paturi, A. Aho, K. Eränen, J. Hemming, M. Peurla, D.
961   Kubička, I. L. Simakova, and D. Yu. Murzin, Hydrodeoxygenation of isoeugenol over Ni- and
962   Co-supported   catalysts,   *ACS   Sust.   Chem.   Eng.,*   **2019**,   *7*,   14545-14560,   DOI:
963   10.1021/acssuschemeng.9b02108.

964   41.   M. E. Martinez-Klimov, P. Mäki-Arvela, Z. Vajglová, M. Alda-Onggar, I. Angervo, N.
965   Kumar, K. Eränen, M. Peurla, M. H. Calimli, J. Muller, A. Shchukarev, I. L. Simakova, and D.
966   Yu. Murzin. Hydrodeoxygenation of isoeugenol over carbon-supported Pt and Pt-Re catalysts
967   for production of renewable jet fuel, *Energy & Fuels,* **2021**, *35*, 17755-17768, DOI:
968   10.1021/acs.energyfuels.1c02656.

969   42.   S. M. Li, B. Y. Liu, J. Truong, Z. Y. Luo, P. C. Ford, and M. M. Abu-Omar, One-pot
970   hydrodeoxygenation (HDO) of lignin monomers to C9 hydrocarbons co-catalysed by Ru/C and
971   Nb_2O_5, *Green Chem.,* **2020**, *22*, 7406-7416, DOI: 10.1039/d0gc01692f.

972   43.   N. Joshi, and A. Lawal, Hydrodeoxygenation of 4-Propylguaiacol (2-Methoxy-4-
973   propylphenol) in a microreactor: performance and kinetic studies, *Ind. Eng. Chem. Res.,* **2013**,
974   *52*, 4049-4058, DOI: 10.1021/ie400037y.

975   44.   I. L. Simakova, Z. Vajglová, P. Mäki-Arvela, K. Eränen, L. Hupa, M. Peurla, E. M.
976   Makila, J. Warna, and D. Yu. Murzin, Citral-to-menthol transformations in a continuous reactor
977   over Ni/mesoporous aluminosilicate extrudates containing a sepiolite clay binder, *Org. Proc.*
978   *Res. Dev.,* **2022**, *26*, 387-403, DOI: 10.1021/acs.oprd.1c00435.

979   45.   G. Ertl, H. Knözinger, F. Schüth, J. Weikamp, *Handbook of Heterogeneous Catalysis*;
980   Wiley-VCH Verlag GmbH & Co. KGaA, 2008, DOI: 10.1002/9783527610044.hetcat0001.

981   46.   D. Yu. Murzin, *Chemical Reaction Technology*; De Gruyter, 2022.

982   47.   S. H. Fogler, *Elements of Chemical Reaction Engineering*; Pearson, 2020.

983   48.   Y. Li, C. S. Zhang, Y. G. Liu, S. S. Tang, G. H. Chen, R. Q. Zhang, X. Q. Tang, Coke
984   formation on the surface of Ni/HZSM-5 and Ni-Cu/HZSM-5 catalysts during bio-oil
985   hydrodeoxygenation, *Fuel,* **2017**, *189*, 23-31, DOI: 10.1016/j.fuel.2016.10.047.

986   49.   R. Olcese, M.M. Bettahar, B. Malaman, J. Ghanbaja, L. Tibavizco, D. Petitjean, A.
987   Dufour, Gas-phase hydrodeoxygenation of guaiacol over iron-based catalysts. Effect of gases
988   composition, iron load and supports (silica and activated carbon), *Appl. Catal. B*, **2013**, *129*,
989   528-538, DOI: 10.1016/j.apcatb.2012.09.043

990   50.   K. Routray, K.J. Barnett, G.W. Huber, Hydrodeoxygenation of pyrolisis oils, *Energy*
991   *Technol.*, **2016**, *5*, 80-93, DOI: 10.1002/ente.201600084